



HAL
open science

Anisotropy in cyclic behavior and fatigue crack growth of IN718 processed by laser powder bed fusion

Mélanie Prost, Alain Köster, Djamel Missoum-Benziane, Sylvain Dépinoy,
Lyliat Ferhat, Matthieu Rambaudon, Vincent Maurel

► **To cite this version:**

Mélanie Prost, Alain Köster, Djamel Missoum-Benziane, Sylvain Dépinoy, Lyliat Ferhat, et al..
Anisotropy in cyclic behavior and fatigue crack growth of IN718 processed by laser powder bed fusion.
Additive Manufacturing, 2022, 61, pp.103301. 10.1016/j.addma.2022.103301 . hal-03935142

HAL Id: hal-03935142

<https://hal.science/hal-03935142>

Submitted on 27 Jan 2023

HAL is a multi-disciplinary open access archive for the deposit and dissemination of scientific research documents, whether they are published or not. The documents may come from teaching and research institutions in France or abroad, or from public or private research centers.

L'archive ouverte pluridisciplinaire **HAL**, est destinée au dépôt et à la diffusion de documents scientifiques de niveau recherche, publiés ou non, émanant des établissements d'enseignement et de recherche français ou étrangers, des laboratoires publics ou privés.

Anisotropy in cyclic behavior and fatigue crack growth of IN718 processed by laser powder bed fusion

Mélanie Prost^a, Alain Koster^a, Djamel Missoum-Benziane^a, Sylvain Dépinoy^a, Lyliat Ferhat^a, Matthieu Rambaudon^a, Vincent Maurel^{a,1}

^aMINES Paris, PSL Research University, MAT - Centre des Matériaux, CNRS UMR 7633, BP 87 91003 Evry, France

Abstract

This study aims at characterizing the role of strong anisotropy in fatigue crack growth for a superalloy processed by additive manufacturing. The choice has been made to investigate two specimens exhibiting significantly different crystallographic textures, representative of possible variations of microstructures within a real part.

Both cyclic mechanical behavior and fatigue crack growth have been investigated at high temperature. As a consequence of the oriented microstructure, high levels of anisotropy of elastic and viscoplastic behaviors were observed. These behaviors have been modeled by the combination of orthotropic elasticity, a Hill's criterion and linear and non-linear kinematic hardening laws. To assess fatigue crack growth driving forces, in the context of complex crack shape, finite element analysis was proceeded taking care of 3D crack shape description. J was derived from $G-\theta$, this method being convenient for anisotropic material.

In most cases, fatigue cracks were found to grow preferentially at the vicinity of grain boundaries, regardless of the crystallographic orientation. An intrinsic fatigue crack growth rate related to this intergranular mechanism has been determined. On the other hand, mostly transgranular crack growth were observed when the loading was applied in the processing direction. In this case, the crystallographic texture appears to be the main factor governing the fatigue crack growth rate.

Keywords: Fatigue crack growth, L-PBF, anisotropy, J-integral, $G-\theta$

Contents

1	Introduction	3
2	Material, specimens and methods	4
2.1	Processing parameters and heat treatment	4
2.2	Microstructural characterizations	5
2.3	Mechanical characterizations	5
2.4	Fatigue crack growth tests	5
2.5	The $G-\theta$ method	8
3	Microstructures of interest	9
4	Mechanical behavior of L-PBF IN718	10
4.1	Experimental mechanical behavior	10
4.2	Mechanical behavior modeling	12

*Corresponding author. Tel.: +33-1-60 76 30 03; Fax: +33-1-60 76 31 50
E-mail address: vincent.maurel@mines-paristech.fr

5	Fatigue crack growth analysis	15
5.1	The DS-like material - set of parameters A	15
5.2	The "more isotropic" material - set of parameters B	22
6	Fatigue crack growth assessed by FEA	24
6.1	Crack morphology and growth	24
6.2	Driving forces assessed from $G-\theta$	25
6.3	Fatigue crack growth rate for DS-like material: influence of the orientation	25
6.4	The role of AM anisotropic microstructure on fatigue crack growth rate	27
7	Conclusion	28
Appendix A		29
Driving force from $G-\theta$		29
Appendix B		29
Analysis of Paris' law from data formulated in ΔK to ΔJ		29

Highlights

- IN718 was processed by L-PBF for two sets of processing parameters, yielding one or two main grains orientations
- Resulting mechanical behavior is strongly anisotropic for both elasticity and cyclic hardening
- Fatigue crack path is mostly governed by grain boundaries, with the exception of tests conducted with loading in the building direction.
- Complex crack morphology implies that driving forces can only be retrieved through 3D finite element analysis (FEA) accounting for anisotropy
- Integral-J assessed by FEA reveals an almost intrinsic behavior for intergranular cracking
- Crystallographic texture impact strongly fatigue crack growth rate in the case of transgranular cracking

1. Introduction

Laser powder bed fusion (L-PBF) is the most investigated additive manufacturing (AM) technology since it enables the design of complex geometries and multi-functions associated to them. Early attempts of manufacturing parts by L-PBF often resulted in a suboptimal compacity, and a hot isostatic pressure (HIP) post-treatment was mandatory to avoid any detrimental effect of pores in fatigue lifetime (e.g. [1]). Due to significant process optimizations, most of the L-PBF materials processed nowadays exhibit a pore fraction that lies within industrial standard ranges, i.e. below 0.1% [2].

The large thermal gradients and fast solidification rates stemming from the L-PBF process lead to columnar grains oriented in the processing direction. As a consequence, a preferential crystallographic texture is observed [3, 4]. It has been shown that recrystallization post-treatment could yield isotropic microstructures, leading to properties reaching those of cast alloys with similar composition when tested in fatigue [5, 6]. However, the anisotropy induced by AM could be kept for both economic and material design purposes. A strong anisotropy is beneficial for some applications (e.g. blades and vanes for aeronautic application), as it optimizes mechanical properties in a given direction. AM technology can thus be used to mimic directionally solidified (DS) alloys or single crystal superalloys [7], with fatigue properties comparable to standard cast single crystal [8]. Furthermore, L-PBF paves the way for otherwise unobtainable design possibilities such as internal holes, thin tubes used for cooling/heat exchanger, lattice structure of complex geometry, and thin walls of materials. In such cases, the as-processed microstructure can significantly vary within a single part depending on its local geometry. Indeed, local solidification conditions are known to be a function of the processed part geometry. In such conditions, a final part may present a broad variety of crystallographic textures and grain size, and thus of mechanical properties.

Damage tolerance analysis is known to increase the range in which materials can be used. Thus, the impact of fatigue crack growth must be assessed for materials exhibiting as-processed crystallographic textures. In this framework, IN718 is a good candidate to represent face-centered cubic (FCC) superalloys. Indeed, optimal process parameters for IN718 are well-known, meaning that a very low fraction of pores can be easily reached [9].

Recently, it has been found that similar heat treatments conducted with or without HIP showed similar fatigue crack growth rates (FCGR) and crack growth path using compact tension (CT) specimens to investigate the long crack regime at room temperature [10]. CT specimens are straightforward to analyze this regime since they limit the plasticity levels in mode I. The fatigue crack growth behavior was further investigated by Ma et al., who have analysed the effects of orientation and temperature on the fatigue short crack growth behavior of L-PBF IN718 by in situ scanning electron microscopy (SEM) testing [11]. Fatigue crack growth rates showed remarkable fluctuations for all testing cases. The deceleration was closely related to the hindering effect of grain boundaries, and a subsequent acceleration was found after overcoming the microstructural barriers or coalescence with adjacent cracks. The fatigue short crack growth rates of L-PBF IN718 alloy showed evident orientation dependency: fatigue cracks propagated much faster in the V-specimens, corresponding to loading parallel to the building direction, than that of the two other orientations (H and 45, respectively orthogonal and forming a 45° angle between loading and building directions). The authors concluded that this effect was mostly due to the small misorientations between adjacent grains for the V-specimen, which followed a cube texture, and to the lower strength along the building direction. The 45-specimens showed lower fatigue crack growth rate (FCGR) than that of H specimen at room temperature, this effect being limited at 650 °C [11]. These points need clearly to be completed by fatigue crack growth analysis for longer cracks in the context of fully anisotropic IN718 processed by L-PBF. Besides, as observed in most studies dealing with FCGR in superalloys processed by additive manufacturing, oversimplification of stress intensity factor (SIF) analysis were used, ignoring to a large extent the role of anisotropy in the assessment of driving forces for crack growth.

As a summary, very few studies are addressing the short to small crack propagation regime at high temperature, that is to say the transition to long crack regime. Furthermore, most of them ignore the interactions between crack and plasticity in the case of anisotropy, and subsequently the associated fatigue crack growth mechanisms. As a consequence, driving forces for fatigue crack growth in the context of fully anisotropic IN718 processed by L-PBF remain to be investigated.

The aim of this paper is to use L-PBF to induce different level of microstructural, and thus mechanical, anisotropy, that are representative of the variety of microstructures encountered in real parts. First, microstructural and mechanical characterizations are developed. Fatigue crack growth paths are investigated in light of this anisotropy, allowing to the determination of the fatigue crack growth mechanisms. In order to incorporate the effect of modal mixity associated to

crack deviation, a 3D model of crack path has been carried out combined to non-linear and linear kinematic hardening anisotropic behavior. Finally, some guidelines for damage tolerance analysis in the scope of finite element analysis (FEA) of fully anisotropic material are detailed through fatigue crack growth rate analysis.

2. Material, specimens and methods

2.1. Processing parameters and heat treatment

An INCONEL 718 powder which grain size ranges from 20 to 45 μm , with a mean size of 33 μm , was used in this study. Specimens were processed using a CONCEPT LASER M2 facility. An Argon atmosphere was used to prevent the detrimental oxidation of the parts during processing. A 45/45 scanning laser strategy was chosen to maximize in-plane isotropy and three main process parameters were varied: laser power (P), scan speed (v) and hatch spacing (Ev); the spot size (Φ) being kept as a constant. In the following, the building direction is referred to as the Z-axis, while the XY plane corresponds to the slice plane.

Table 1: Process parameters and measured porosity

	Power (W)	Speed (mm/s)	Ev (mm)	Φ (mm)	Laser energy (J/mm)	Surface porosity (%)
Parameters-A	250	800	0.105	0.180	0.31	0.07
Parameters-B	370	700	0.130	0.180	0.53	0.04

Two sets of process parameters, with large difference in linear energy, were selected for this study (table 1). The porosity for each set of parameters was measured by image analysis on a surface of about 4.7 mm^2 cut from a 10x10x10 mm^3 cube. From optical observation, Figure 1a, segmentation gives access to the pore surface and thus porosity, Figure 1b. Similar observations have been carried out on each external surface of the specimen used for mechanical testing (in particular heads and lateral side observed in situ). For each set of parameters, the porosity measured from the cube was the highest. The measured porosity was found to be rather low, i.e. 0.07% and 0.04% for Parameters A and B respectively.

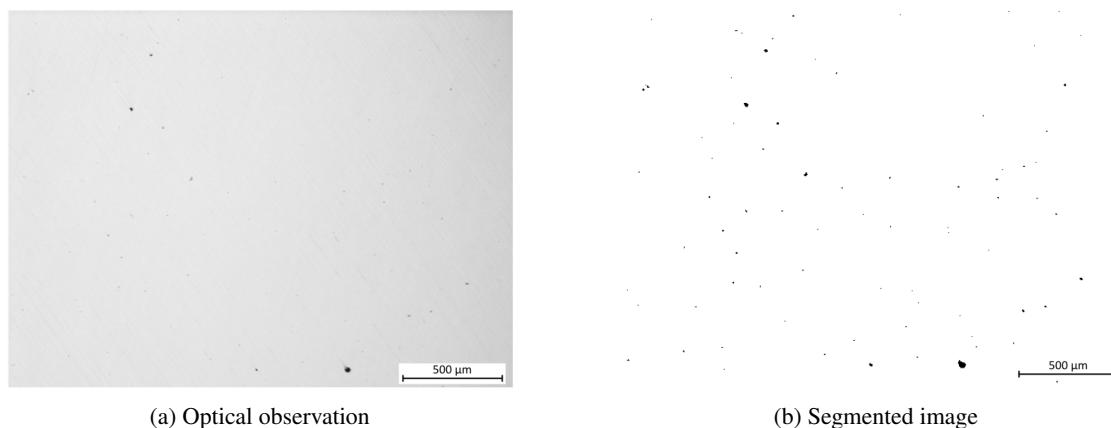


Figure 1: Porosity measurement on top surface of cube, here for the set of parameters B

The chemical composition of the powder is given in table 2, and meets the standard range for IN718 alloy.

Table 2: Composition of L-PBF IN718

Elements	Ni	Cr	Fe	Nb	Mo	Ti	Al	Si
Weight (%)	bal.	19.20	18.01	6.18	3.35	1.18	0.47	0.11

A so-called "direct aging" (DA) heat treatment has been applied for the L-PBF IN718 processed material. DA is known to improve mechanical properties of wrought IN718 for creep, fatigue and fatigue crack propagation [12, 13, 14, 15, 16]. Besides, significant residual stress relaxation is observed after DA [17]. This heat treatment consists in a first isothermal step at 720 °C for 8 h, then a furnace cooling with a cooling rate set to 100 °C/h. When specimens have reached 620 °C, the temperature is kept constant for 10 h with a final air cooling step. For L-PBF IN718, it has been shown recently that the anisotropy observed in the as-processed condition was kept after a DA heat treatment [18].

2.2. Microstructural characterizations

Grain morphologies and crystallographic textures for both processing conditions were studied by electron backscatter diffraction (EBSD). EBSD analyses were carried out in a ZEISS SIGMA-300 SEM, using a NORDIFF detector with a 20 kV acceleration voltage and a 2 µm step size. Prior to EBSD analysis, samples underwent standard metallographic preparation with a final OPS polishing. Optical observations were performed after etching the sample with a 10% solution of oxalic acid in water, using a 5 V current for 7 seconds.

2.3. Mechanical characterizations

Mechanical behavior characterizations were performed on smooth cylindrical specimens with a gage length of 12 mm and a diameter of 4 mm. After AM process and DA heat treatment, the samples were machined and polished to decrease the surface roughness down to 1 µm using diamond paste. Three samples orientations were designed for the characterization of the mechanical behavior: one parallel to the Z-direction with the XY-plane orthogonal to its axis (V-sample), one with the XY-plane parallel to its axis (H-sample), and one aligned with a direction forming a 45° angle with XY-plane (45-sample).

The whole tests serie has been carried out at 550 °C, using a four bulbs lamp furnace. The temperature was controlled by a K-type thermocouple welded to the specimen. Tests were strain controlled using contact extensometer designed for high temperature, with extensometer arms made of alumina [19].

Cyclic hardening and stress relaxation were characterized in a wide range of strain using a single specimen, thanks to the use of incremental straining steps during the test, as proposed in [20]. The cycling can be described, for a given strain level, as follows: (i) an increase in strain up to a strain value ϵ_i in 2.5 s, followed by (ii) a dwell at ϵ_i during 300 s, and (iii) a decrease down to $-\epsilon_i$ in 5 s. This procedure was repeated 10 times for each targeted strain level ϵ_i , from 0.2 % to 1.25 %.

These tests were handled for all sample orientations, V, H and 45-samples, and for the two sets of processing parameters. Each mechanical test condition and associated specimen will be referred to as M-orientation-parameters in the sequel: e.g. M45-A corresponds to a 45° sample (loading applied at 45° to the building direction) and set of parameters A and MV-B corresponds to a V sample (loading applied in the building direction) and set of parameters B.

2.4. Fatigue crack growth tests

Single edge notch tension (SENT) specimens were used to promote the crack growth sensitivity to microstructural heterogeneity, from short to small crack, e.g. see [21]. The chosen geometry is detailed in Figure 2. SENT specimens were used with a gage length of 12 mm wide and 3 mm thick. The notch was processed by electro discharge machining (EDM), and exhibits a length of 800 µm for a width of about 200 µm. After AM and DA heat treatment, the samples were machined and polished to eliminate the surface roughness, down to 1 µm using diamond paste.

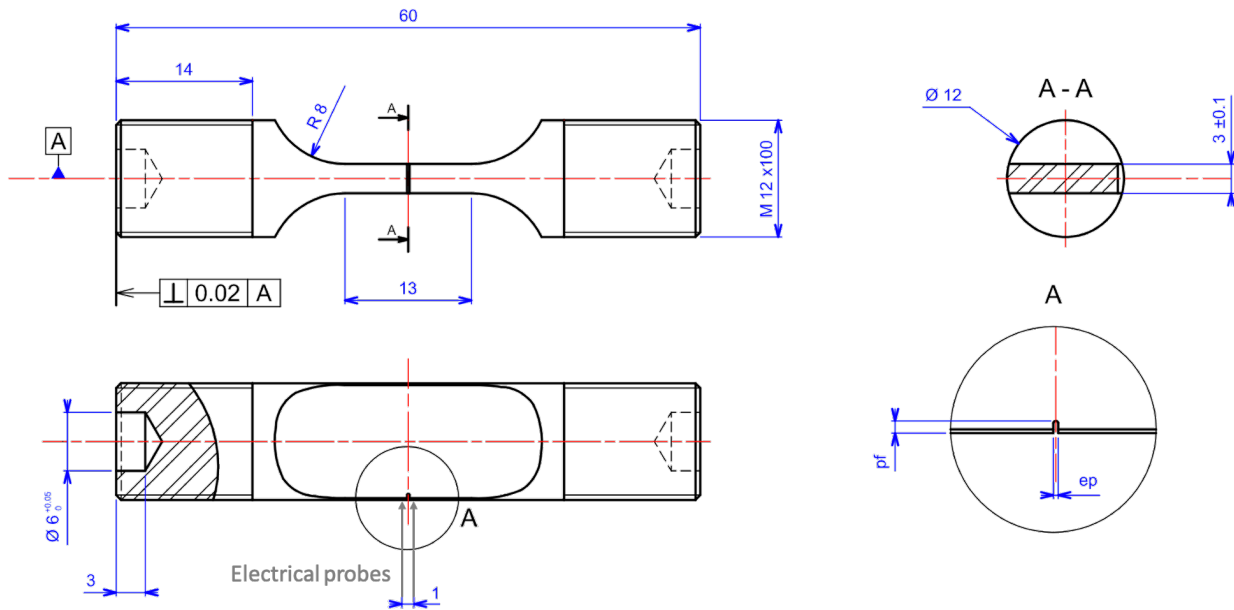


Figure 2: SENT geometry (dimensions in mm); for the notch, the length pf is set to $800 \mu\text{m}$ and the width ep to $200 \mu\text{m}$

Similarly to mechanical behavior characterizations, SENT specimens have been built in three configurations: V, H and 45, Figure 3. Each fatigue crack growth test condition and associated specimen will be referred to as F-orientation-parameters in the following: e.g. F45-A corresponds to a 45° sample (loading applied at 45° to the building direction) and set of parameters A and FV-B corresponds to a V sample (loading applied in the building direction) and set of parameters B. It is worth noting that the root of the notch will impact the orientation of crack initiation with respect to layers, highlighted in blue, and loading direction; see details in Figure 3. To summarize, FV, F45 and FH specimens correspond to XY-building planes being respectively orthogonal, oriented at 45° , and parallel with respect to the loading direction.

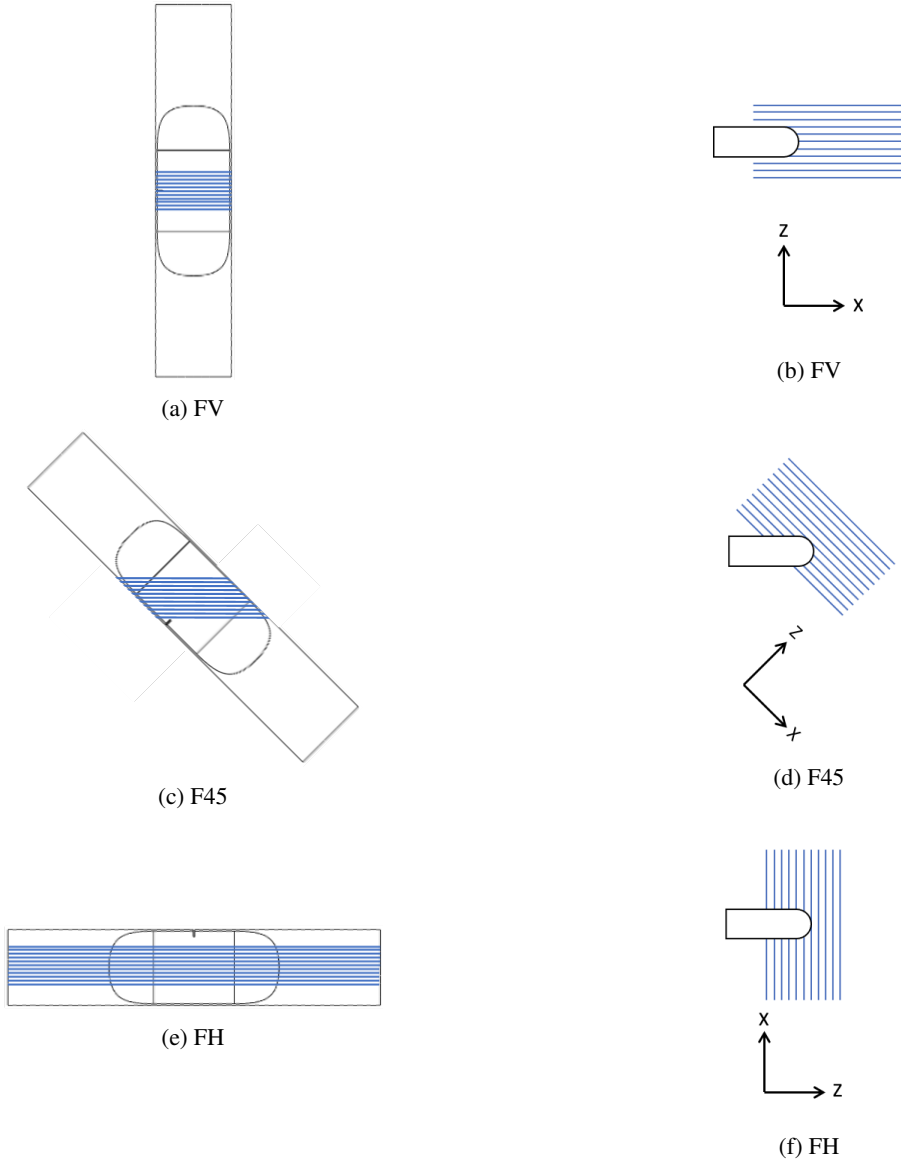


Figure 3: Sketch of SENT samples used for mechanical testing (a), (c) and (e) and detail of notch (b), (d) and (f) according to the trace of slicing planes (in blue) assumed to be orthogonal to the Z-direction.

Fatigue crack growth tests (FCG) were conducted using the same facility used for mechanical behavior characterization. Tests were performed at 550 °C and controlled by force, using a loading ratio $R_\sigma = 0.1$ and a triangular signal set to 1 Hz, following standard practice [22]. The force was adjusted such that FCG tests started at an initial amplitude of the stress intensity factor (SIF) value of $15 \text{ MPa}\sqrt{m}$. The SIF value was assessed by considering the notch length as the crack length in the expression of mode I analysis of SENT specimen [23] (see also [24, 25]):

$$\Delta K = \Delta\sigma \left(1.122 + 0.5 \frac{a}{w} \right) \sqrt{\pi a} \quad (1)$$

where w corresponds to the specimen width. This assumes elastic and isotropic behavior. At this point, by ignoring impact of anisotropy on SIF value at crack initiation, one should only consider this as a rough approximation of the starting value of ΔK . This assumption will be discussed in section 6.

Crack growth was monitored by potential drop technique (PDT) and in-situ optical microscopy surface crack

measurement. Similar set-ups are detailed in [26]. The two electrical probes needed for potential drop technique measurement were welded symmetrically around the notch, and are distant of 1 mm, Figure 3. The precise distance between probes was checked for each specimen. PDT yields a global and continuous measurement of the cracked area, whereas optical observation yields local information on one side of the specimen. A second order polynomial fit is used to describe the PDT evolution and is calibrated to fit with surface measurement.

The roughness of the fractured surfaces were measured using an optical profilometer ALTISURF 500 (ALTIMET, France). The associated height and lateral resolutions are of about 0.1 μm and 3 μm respectively.

2.5. The G- θ method

Driving forces for crack growth analysis were derived using numerical method associated to finite element analysis (FEA) using the Zset software [27].

As a standard of fatigue crack growth analysis, either the amplitude of SIF or J-integral values could be analysed. The latter is known to be convenient for anisotropic material and for the most general cases of complex crack geometries. For FEA, the analysis of J from G- θ as proposed by [28], corresponds, in absence of volume force, to:

$$G_h = \frac{1}{S} \left[\int_{\Omega} \left(\sigma_{ij} u_{i,j} \theta_{j,k}^h - W \theta_{i,i}^h + \sigma_{ij} \alpha \Delta T \theta_{i,j}^h \right) d\Omega \right] \quad (2)$$

where σ_{ij} denotes the stress tensor components with indexes ij varying in $[1, 2, 3]$, u_i refers to displacement components in direction i , $u_{i,j}$ corresponds to its spatial derivation along the coordinate x_j using summation of indexes. The main ingredient of the method is the virtual displacement field of the crack front θ_i^h , where h corresponds to crack propagation mode I, II or III, assessed when the virtual displacement field is respectively normal to the front (N), along the binormal of the front (B) and tangential to the front (T), Figure 4. W corresponds here to the total strain energy $W = \int \sigma_{ij} \epsilon_{ij} d\Omega$. Finally, the local variation of temperature, ΔT is also accounted for, but is of no impact considering the isothermal and homogeneous temperature condition used in this study. This method is straightforward also in presence of plasticity [29, 30].

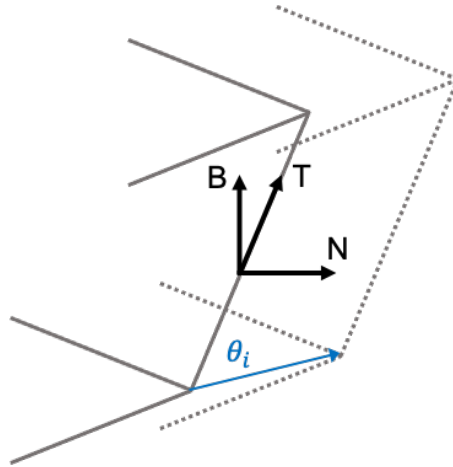


Figure 4: Illustration of virtual displacement field with local axes at a point of the crack front (normal to the front (N), along the binormal of the front (B) and tangential to the front (T))

Thus, direct projections of θ vector onto normal, bi-normal and tangent local axes yield access to G_I , G_{II} and G_{III} , respectively. The above expression of G_h ignores the coupled term $\int_{\Gamma_N} [[W]]^{\pm} n_k$ discussed in [31]. This term has been seen to be highly sensitive to contact algorithm, whereas in our cases asymptotic values of G_{II} and G_{III} are obtained for a sufficient number of layers used in the volume integral, see details in AppendixA. Together with the crack tip location, FEA yields the values of G_i from G- θ method. A classical approximation is proposed to assume that $J_i = G_i$, for $i=I, II, III$, respectively associated to crack opening, in plane crack shear and out-of-plane modes, accounting for 3D shape of the crack [28]. The analysis of driving forces for crack growth was based on G- θ in this study, including the full anisotropic elasto-viscoplastic model as described below.

3. Microstructures of interest

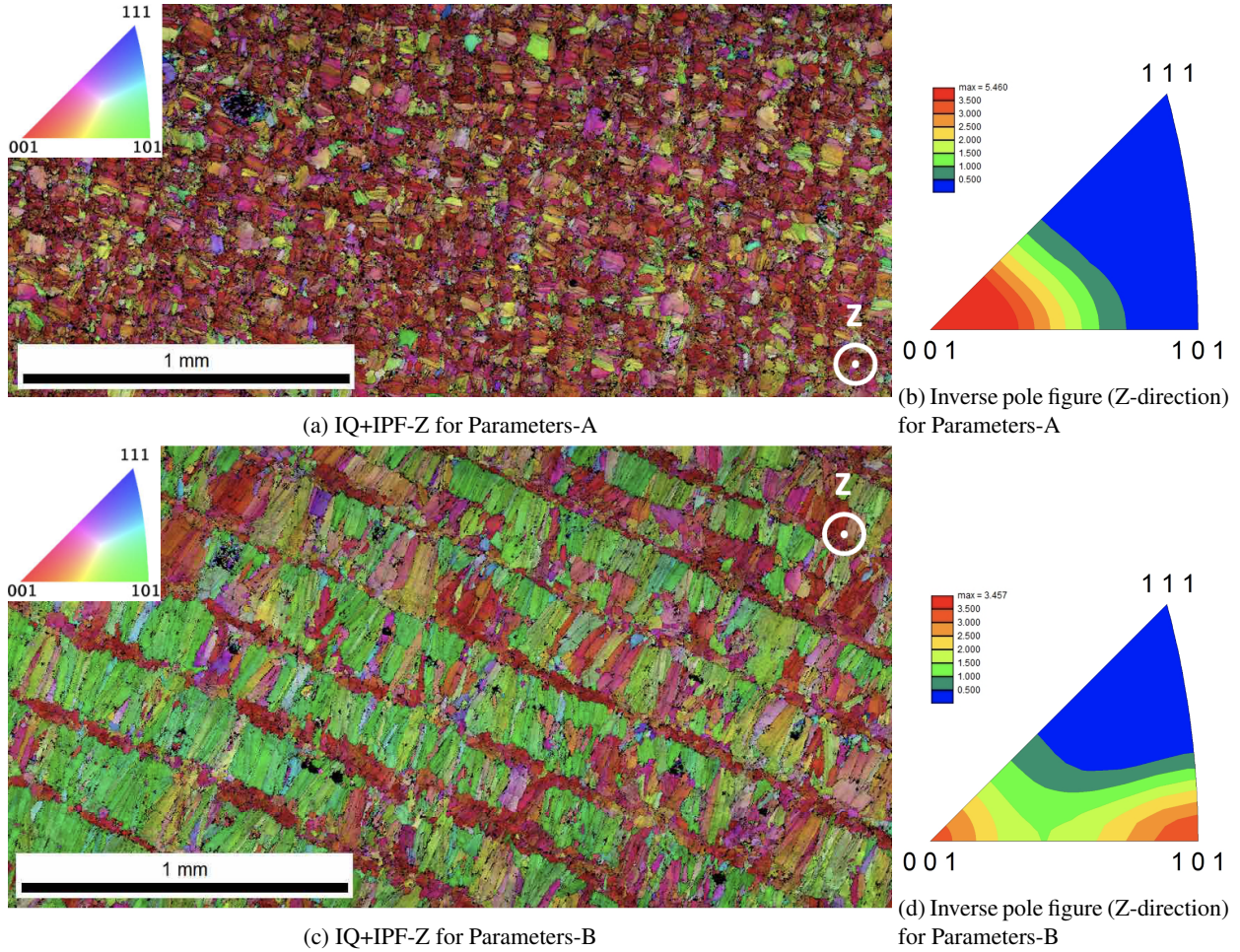


Figure 5: EBSD measurements in planes orthogonal to the processing direction, Z for set of parameters A and B

The two chosen microstructures are significantly different, as expected from the choice of process parameters. In the XY-plane, Parameters-A material exhibits small and regular grains, close to square shape, with refined grains in orthogonal bands, Figure 5a. On the other hand, Parameters-B material exhibits elongated cross-sections of grains together with refined grains located in bands in the scanning direction, Figure 5c. The most noticeable aspect of these microstructures is related to clear differences in their crystallographic orientations: for Parameters-A most of grains are observed in $\langle 001 \rangle$ orientation with respect to the Z-axis, making this material very close to directionally solidified (DS) alloys, Figure 5b, whereas for Parameters-B two preferential orientations are evidenced by the inverse pole figure, namely $\langle 001 \rangle$ and $\langle 101 \rangle$ with respect to the Z-axis, Figure 5d.

Regardless of the choice of parameters, grains are columnar following the Z-direction, sizing approximately $300 \mu\text{m}$, as is typical for the L-PBF process (Figure 6).

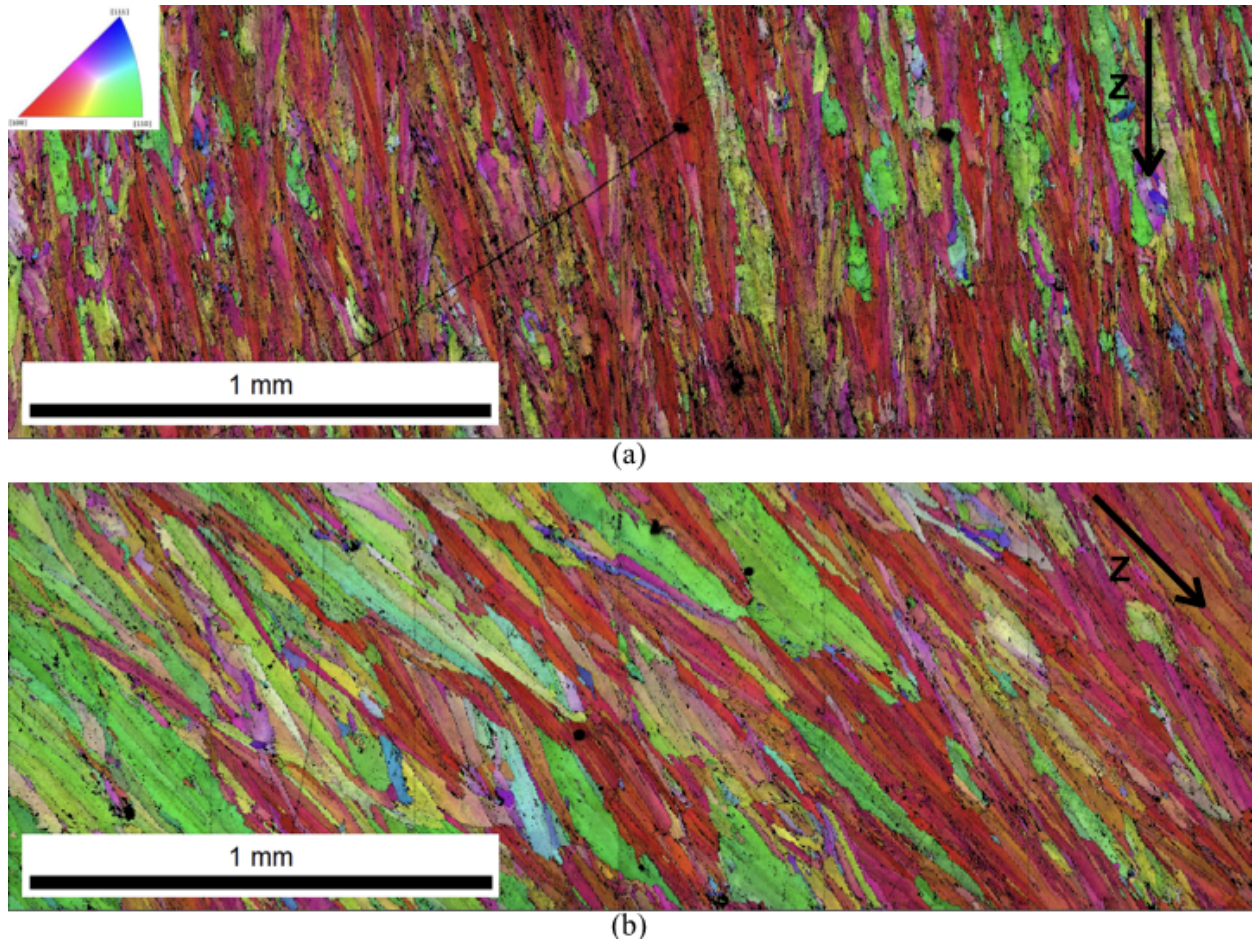


Figure 6: EBSD measurements in planes parallel to the processing direction, Z; IQ+IPF-Z, for (a) Parameters A and (b) Parameters B

These microstructures are in good agreement with the effect of the process parameters on the crystalline texture for FCC materials [32, 33]. It is indeed known that the shape of the melt pool and the overlap between neighbouring laser track change the direction of the thermal gradients and the epitaxial growth, which govern the final texture.

While it is out of the scope of this study to investigate the thermal origins behind the differences between the two specimens, two significantly different microstructures were successfully designed. The set of parameters-A leads to a fully anisotropic microstructure, with only one preferential crystallographic orientation, and the set of parameters-B induces a microstructure with two main orientations, and is therefore expected to be more isotropic. Both microstructures exhibit columnar grains in the Z-direction, although the grain size appears to be smaller for Parameters-A as compared to Parameters-B.

4. Mechanical behavior of L-PBF IN718

4.1. Experimental mechanical behavior

According to the chosen experimental methodology, each targeted maximum strain level is associated with a hysteretic evolution of stress as a function of the applied strain level. For instance, for Parameters-A, it is worth noting that a significant hardening is observed, Figure 7. The stress relaxation is limited to 10% as observed for similar heat treatments for wrought IN718 [34]. This stress relaxation seems to induce a loss of symmetry when comparing maximum positive and minimum negative stress values that is only significant for the M45-A specimen.

The cyclic hardening is also rather limited for the 10 cycles tested. Considering each tested orientation, the mechanical anisotropy is obvious for both elasticity and non-linear hardening, Figure 7.

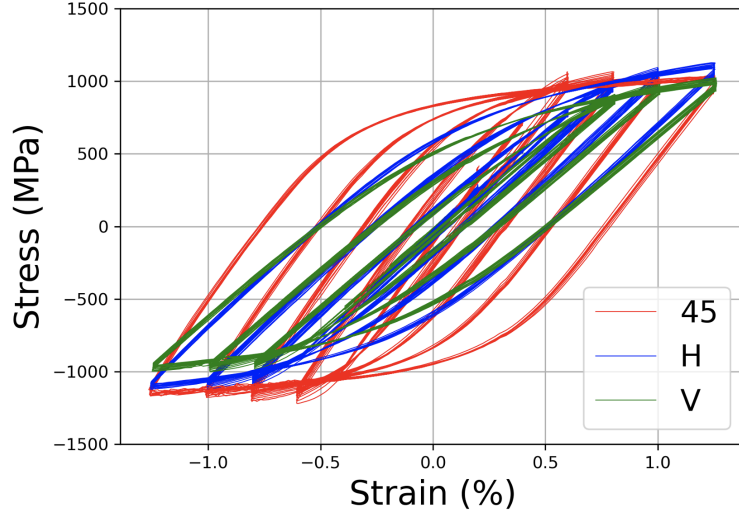


Figure 7: Mechanical behavior for 3 different specimen orientations for Parameters-A

For the sake of clarity, we selected the cycle corresponding to the maximum applied strain level $\Delta\epsilon/2 = 1.25\%$ for both set of parameters A and B, Figures 8a and 8b.

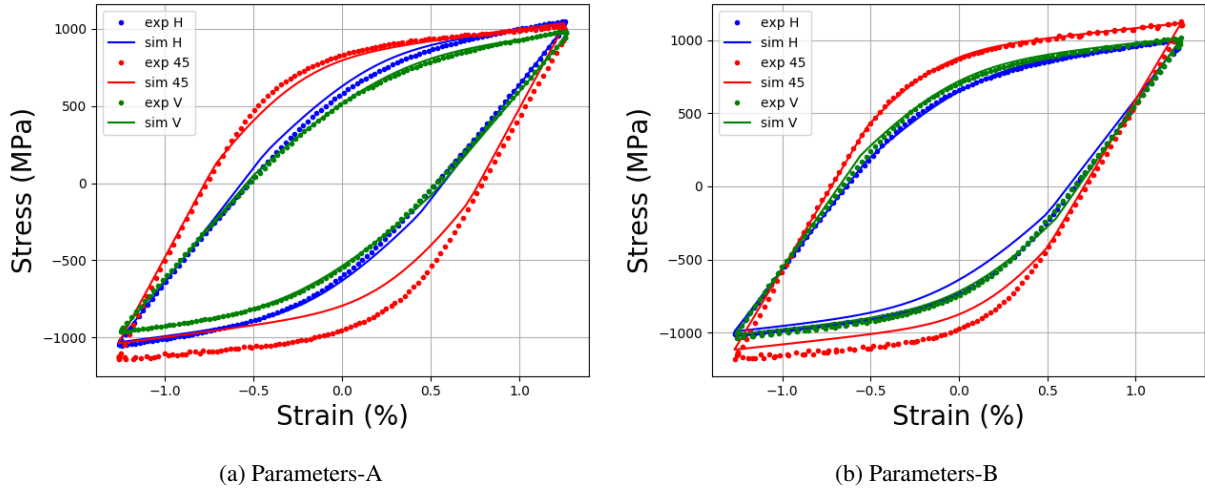


Figure 8: Evolution of stress as a function of strain for the maximum applied strain range $\Delta\epsilon/2 = 1.25\%$, for both set of parameters A and B; experimental (exp) results using symbols and results of simulation (sim) using continuous lines.

For Parameters-A, a strong anisotropy is observed for both elasticity and hardening, see Figure 8a and table 3. Both MH-A and MV-A samples exhibit the lowest Young's modulus and a generally softer behavior compared to the M45-A sample. This M45-A sample appears to be the "hard" orientation of the Parameters-A. This is consistent with its $\langle 001 \rangle$ preferential orientation, Figure 5b. To quantify this sensitivity, the ratio $\Delta E/E_V$ is assessed, see Table 3, where $\Delta E = E_i - E_V$ with E_i corresponding to the Young's modulus of MV, M45 and MH specimen orientation respectively. This ratio is maximized for M45-A, i.e. 64%.

The yield stress of the M45-A sample is higher than for MV-A and MH-A samples. On the other hand, the slope at maximum strain is higher for MH-A and MV-A samples than the one obtained for M45-A sample, see Figure 8a. Using a similar ratio as used for Young's moduli but with $\Delta\sigma/2$, corresponding to $\Delta\varepsilon/2 = 0.2\%$, the maximum is again found for M45-A, i.e. 82%.

For Parameters-B, a less pronounced anisotropic behavior is observed: in comparison with Parameters-A, the maximum ratio in effective Young's modulus drops from 64% to 28%, and the contrast in $\Delta\sigma/2$ at $\Delta\varepsilon/2 = 0.2\%$ drops from 82% to 30%. Note that this maximum ratio nevertheless corresponds to the M45-B compared to the MV-B samples. Considering the slopes up to maximum applied strain in both tension and compression, the hardening is similar for all 3-orientations. But, again, a higher stress value is reached for M45-B sample as compared to MH-B and MV-B samples, associated to a difference in yield stress.

Table 3: Effective Young's modulus and $\Delta\sigma/2$ at $\Delta\varepsilon/2 = 0.2\%$ for the two sets of processing parameters according to the specimen orientation

	Parameters A			Parameters B		
	V	45	H	V	45	H
Young's modulus (GPa)	132	217	147	162	208	206
$\frac{E-E_V}{E_V}$	0	0.64	0.11	0	0.28	0.27
$\Delta\sigma/2$ (MPa)	271	492	301	346	448	434
$\frac{\Delta\sigma-\Delta\sigma_V}{\Delta\sigma_V}$	0	0.82	0.11	0	0.30	0.26

4.2. Mechanical behavior modeling

Let us assume a homogeneous behavior of the materials. To account for both observed elastic anisotropy and viscoplastic anisotropy, orthotropic elasticity and Hill's criterion have been considered respectively [35, 36, 37, 38]. In order to model cyclic hardening, a standard kinematic hardening with a constant isotropic hardening can be used [39]. Here, kinematic hardening is based on the summation of a non-linear, \underline{X}_1 , and a linear, \underline{X}_2 , terms, see Table 4 for constitutive equations. For sake of simplicity, the loss of symmetry only observed in 45 orientation will not be accounted for.

Table 4: Mechanical behavior set of equations. With $\underline{\varepsilon}^{tot}$, $\underline{\varepsilon}^e$ and $\underline{\varepsilon}^p$ the total, elastic and plastic strain tensor respectively, \underline{H} the Hill's tensor assumed to be diagonal, \underline{s} is the deviatoric part of the stress tensor defined by $\underline{\sigma} = \underline{s} + 1/3tr(\underline{\sigma})\underline{1}$, and p is the cumulated plastic strain [40]

Strain partitioning	$\underline{\varepsilon}^{tot} = \underline{\varepsilon}^e + \underline{\varepsilon}^p$
Yield function	$f = \sqrt{\frac{3}{2}(\underline{s} - \underline{X}) : \underline{H} : (\underline{s} - \underline{X})} - R$
Isotropic Hardening	$R = R_0$
	$\underline{X} = \underline{X}_1 + \underline{X}_2$
Kinematic Hardening	$\dot{\underline{X}}_1 = \frac{2}{3}C_1\dot{\underline{\varepsilon}}^p - D_1\underline{X}_1\dot{p}$ $\dot{\underline{X}}_2 = C_2\dot{\underline{\varepsilon}}^p$
Flow Function	$\dot{p} = \left\langle \frac{f}{K} \right\rangle^n$

Based on the whole test series, a least square method associated to a Levenberg-Marquard algorithm yields the optimal set of parameters for the chosen behaviors using the Zset suite [27], see table 5. The identified behaviors are plotted using continuous lines in Figures 8a and 8b.

For plastic behavior, larger deviations from unity of h_2 and h_3 Hill's parameters have been obtained for the set of parameters-A as compared to the set of parameters-B materials. The flow function are chosen with the same parameters for both configurations. The optimized fit is obtained by only modifying the hardening parameters, using the same Norton's parameters (K and n). The chosen hardening laws, combined to the Hill's criterion, are consistent with the observed mechanical behaviors, see figures 8a and 8b.

Table 5: Identified set of parameters for the anisotropic elastic and viscoplastic behavior for both Parameters -A- and Parameters -B materials

(a) Elastic anisotropy parameters ($C_{ij}^{(loc)}$ in MPa)									
	$C_{11}^{(loc)}$	$C_{22}^{(loc)}$	$C_{33}^{(loc)}$	$C_{12}^{(loc)}$	$C_{23}^{(loc)}$	$C_{31}^{(loc)}$	$C_{44}^{(loc)}$	$C_{55}^{(loc)}$	$C_{66}^{(loc)}$
Parameters A	177020	197615	197615	75865	84700	75865	116000	50580	116000
Parameters B	218480	277040	277040	93635	118730	93635	84000	52070	84000

(b) Hardening and flow parameters						
	R_0 (MPa)	C_1 (MPa)	D_1	C_2 (MPa)	K (MPa)	n
Parameters A	510	220000	600	16000	200	2
Parameters B	820	180000	800	14000	200	2

(c) Hill's parameters						
	h_1	h_2	h_3	h_4	h_5	h_6
Parameters A	1.25	0.6	0.6	0.85	1	0.85
Parameters B	2.3	0.9	0.9	1.2	2.1	1.2

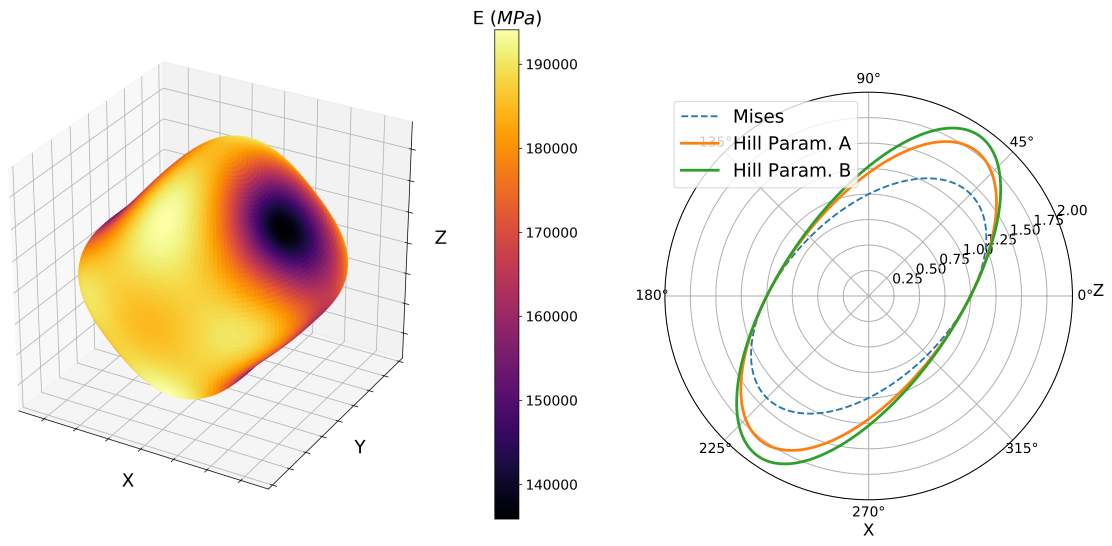
To illustrate the identified material behavior, elastic anisotropy is represented by 3D color sketch of resulting Young's modulus for Parameters-A: for H and V configurations a lower Young's modulus is reached compared to the maximum obtained at 45°, Figure 9a. The level of elastic anisotropy is commonly estimated by considering a coefficient of anisotropy, which is maximized here ¹ for the classical formulation used for quadratic anisotropy:

$$a = \frac{2C_{44}}{(C_{11} - C_{12})} \quad (3)$$

The higher anisotropy observed for Parameters-A compared to Parameters-B results in a higher anisotropy coefficient, respectively $a = 2.3$ and $a = 1.3$. As a mean of comparison, the anisotropy of a single crystal of IN718 is $a = 2.7$ at both room temperature ([41]) and 400 °C ([42]). This confirms that the elastic behavior of the Parameters-A is driven by a single orientation of grains, inducing an anisotropy close to single crystal's one. Similar behavior of Ni-based DS superalloy anisotropy has been observed, e.g. for DS 200 [43], yielding $a = 2.2$. On the other hand the Parameters-B material is closer to isotropic elastic behavior, despite an obvious anisotropic microstructure.

Resulting yield stresses could be observed as a function of applied level of a multiaxial loading: the identified Hill's criterion deviates clearly from Von Mises criterion, for both set of parameters A and B, Figure 9b.

¹i.e. for any other consistent permutation of the indexes of C_{ij} coefficient, the anisotropy coefficient was lower here



(a) Perspective view of anisotropic Young's modulus (Parameters-A)

(b) Hill's criterion for both set of parameters A and B

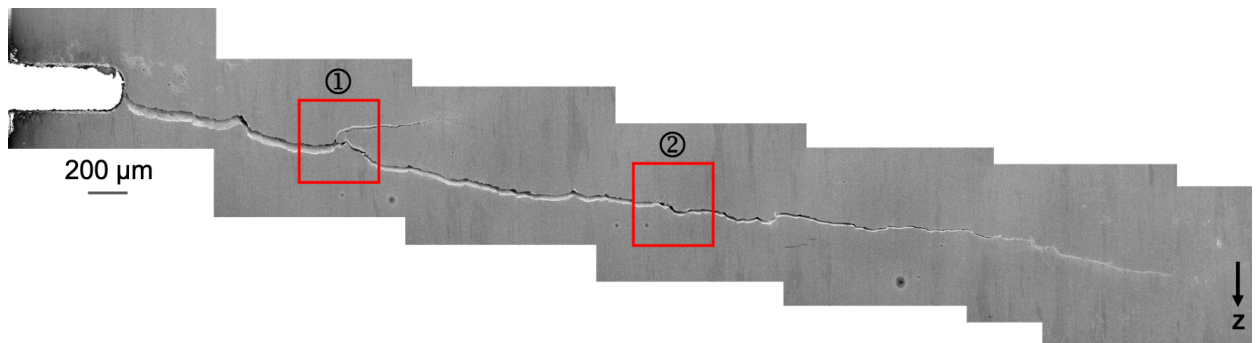
Figure 9: Graphical representation of anisotropic mechanical behavior identified for the L-PBF IN718 highlighting elasticity in (a) through the Young's modulus and plasticity in (b) through the Hill's criterion.

5. Fatigue crack growth analysis

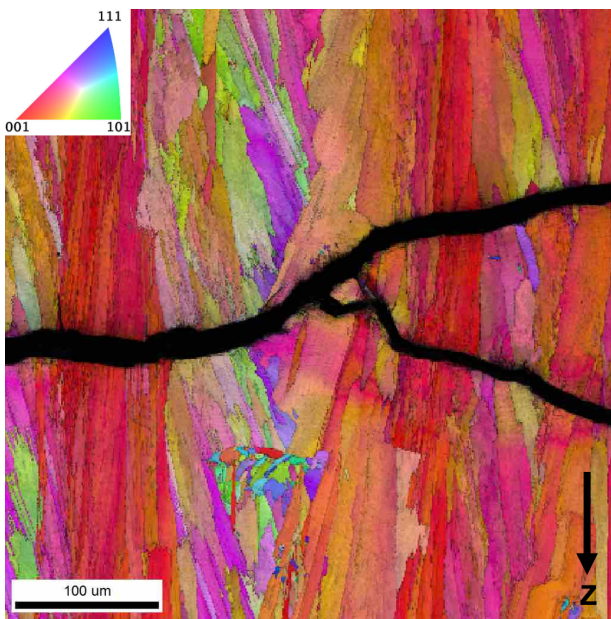
Fatigue crack growth path and fatigue crack growth mechanisms are first analysed for Parameters-A, i.e. the DS-like material. Second, paths are detailed for the Parameters-B, i.e. the more isotropic configuration.

5.1. *The DS-like material - set of parameters A*

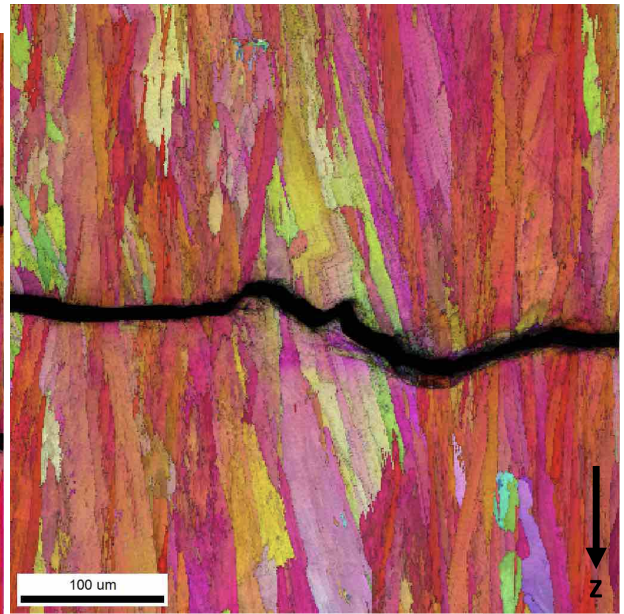
For the FV-A sample, figure 10, the crack path remains almost straight despite deviating early from the plane orthogonal to the loading direction. Crack branching is observed at few different crack locations. As a mean of example, at label ① in Fig. 10a and associated EBSD in Fig. 10b, a secondary crack has grown almost orthogonally from the loading direction, while the major crack kept growing linearly. Neither crack propagation nor crack deviation appear to be correlated to grain boundaries, figure 10b and 10c. Observation of the other side of the specimen shows a crack path almost orthogonal to the loading direction. Thus, a rather limited crack twisting of about 10° is observed, corresponding to the rotation of the crack in the direction of crack growth (see indicative values in table 6). This is confirmed by optical profilometer measurements, 10d, showing a rather smooth fracture surface with low values of tilting and twisting. The twist angle value nevertheless increases with crack growth.



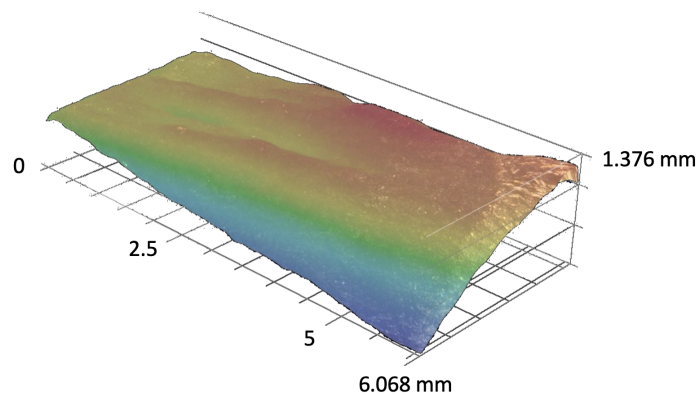
(a) SEM observation along the crack path, red rectangles correspond to EBSD analysis



(b) IPF-Z close to the notch, corresponding to label ① in (a)



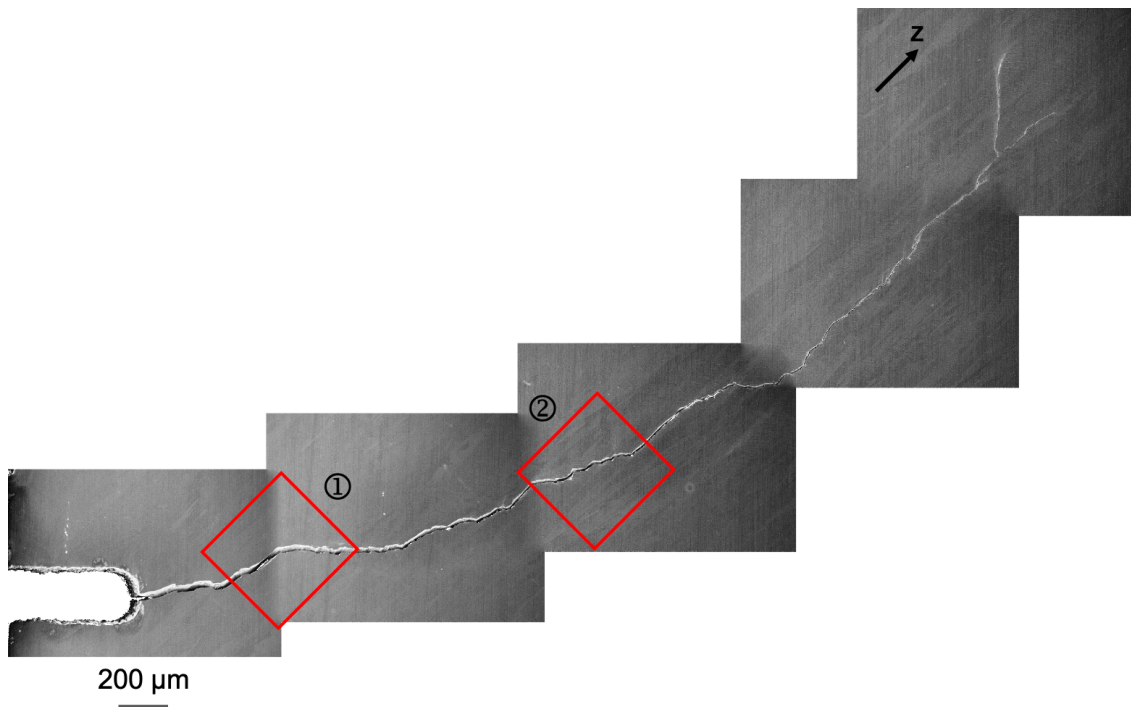
(c) IPF-Z at 3 mm from the notch, corresponding to label ② in (a)



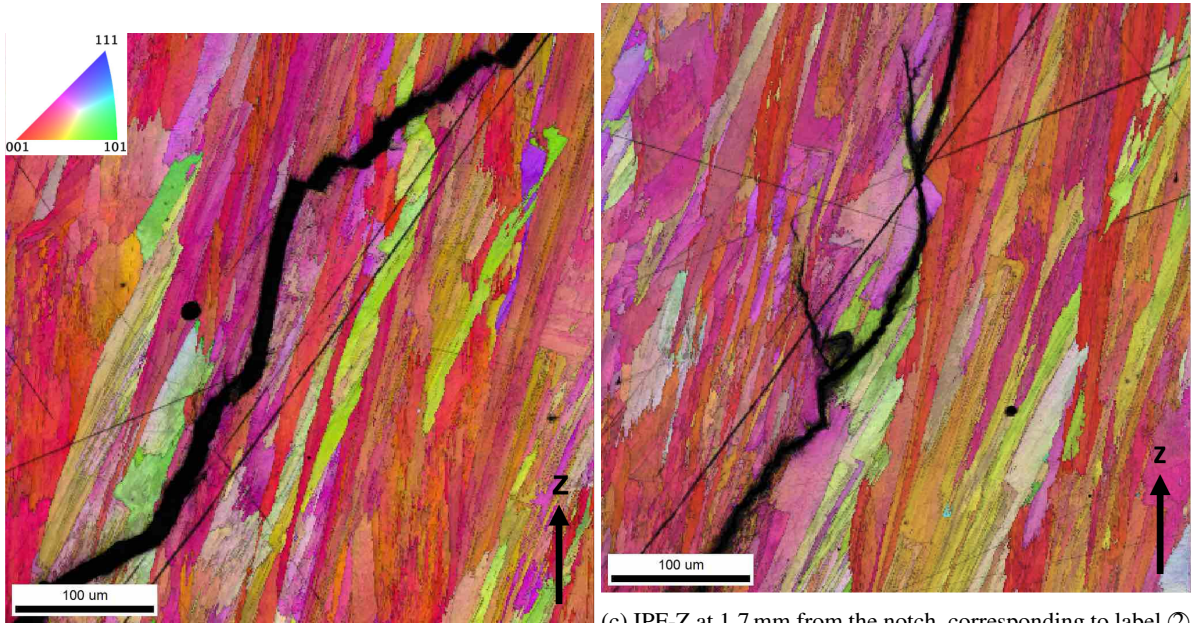
(d) Fractography of FV-A specimen (notch is at abscissa zero)

Figure 10: Crack path of FV-A specimen (a) SEM (secondary electrons) after slight polishing of the surface; (b) and (c) IPF-Z associated to labels in (a); (d) 3D profile of the cracked surface

For the F45-A sample (figure 11), as it grows, the main crack deviates progressively from the direction orthogonal to the loading direction, before stabilising with a 45° angle with respect to the loading direction. Some crack branches are again observed. Crack deviations, figure 11a, crack branching and associated crack arrest, figure 11c, are found close to grain boundaries.



(a) SEM observation along the crack path, red rectangles correspond to EBSD analysis



(b) IPF-Z close to the notch, corresponding to label ① in (a)

(c) IPF-Z at 1.7 mm from the notch, corresponding to label ②

Figure 11: Crack path of F45-A specimen (a) SEM (secondary electrons) after slight polishing of the surface; (b) and (c) IPF-Z associated to labels in (a)

Optical observations are shown in Figure 12, corresponding to the other side of the same specimen. Limited twisting of the crack, of about 15° , is found, while bright areas correspond to strain localizations. At the deviation point (see detailed view ①), slip lines are evidenced within grains, see orange triangle, and along directions consistent

with grain boundaries, see orange arrows. Besides, the upper side of the crack lip does not evidence plastic activity, whereas the grains located in the lower side of the crack lip evidence high shear levels, label ① Figure 12. For longer crack, when the crack path is clearly oriented at 45° (see detailed view ②), some crack branches could be associated to grain boundaries, while other branches could be associated to slip planes within grains.

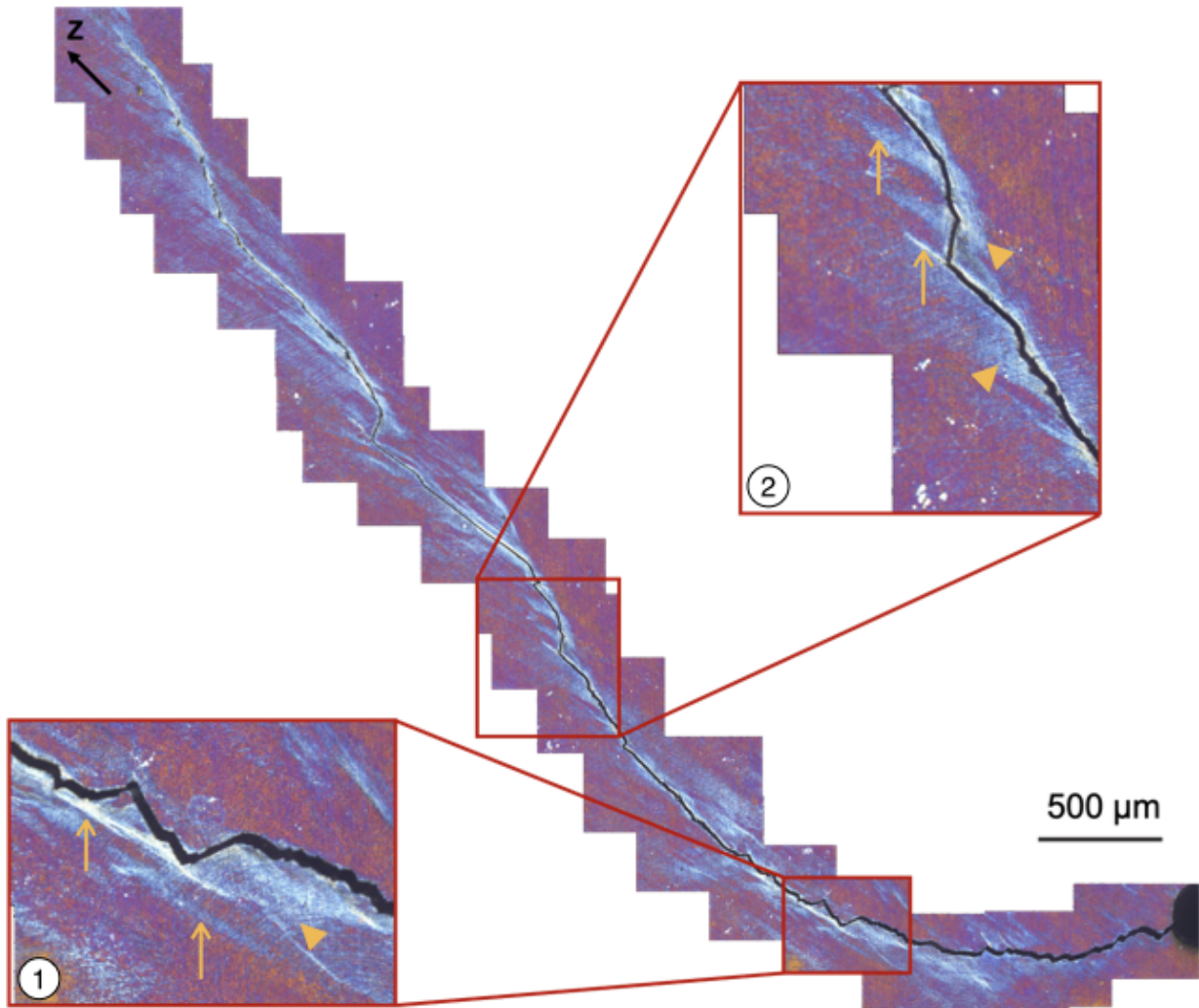
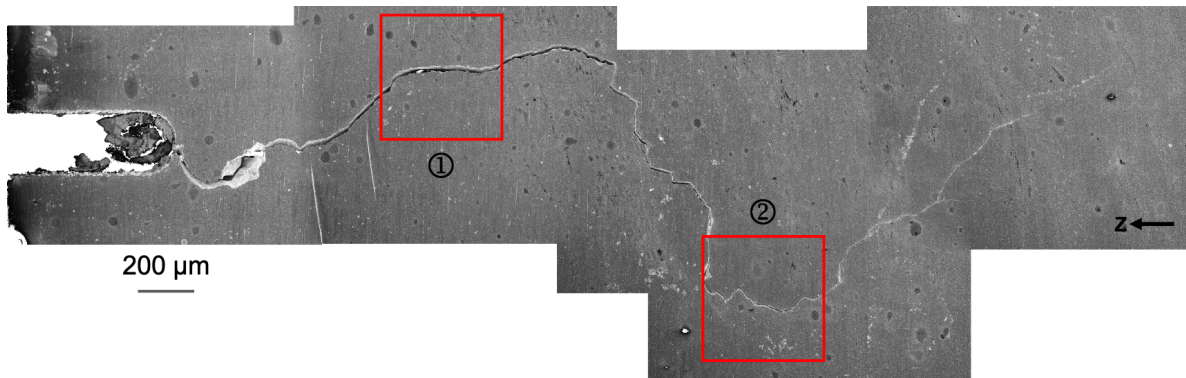
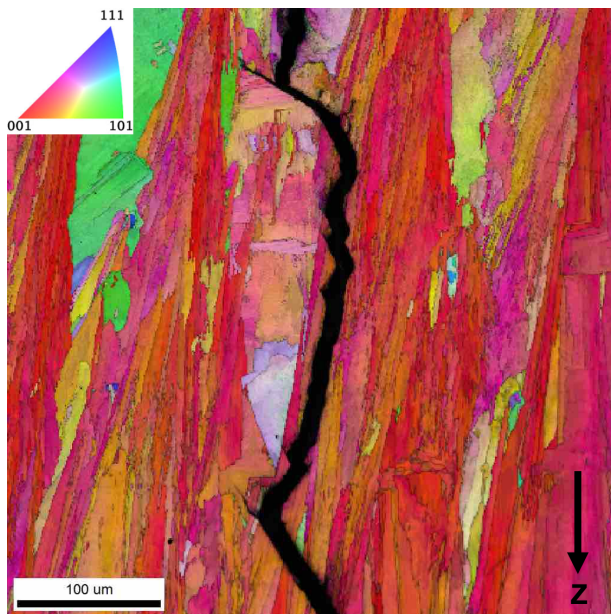


Figure 12: Optical observation along the crack path for F45-A specimen, rectangles correspond to detailed views within which vertical arrows highlight some strain localization and/or cracking at grain boundaries and triangles highlight some areas of intense slip activity within grains

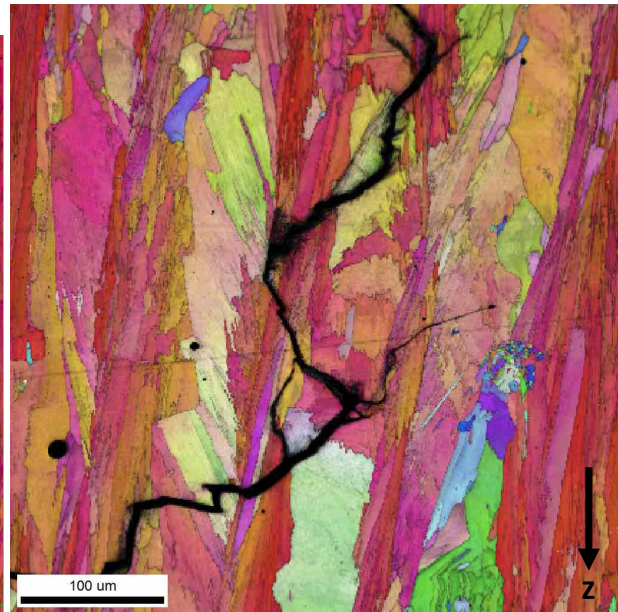
For the FH-A sample (figures 13), crack initiates in the XY-plane, and deviates after a distance of about 100 μm as it crosses successive layers. Up to a crack length of 1.5 mm, the crack is observed to be almost orthogonal to the loading direction, Figure 13a. This crack is observed to be mostly intergranular (or at least in the vicinity of grain boundaries), with local oscillations associated to crack branches along small grains, Figure 13b. Once the crack has propagated enough, large crack oscillations are observed consistently with both larger crack branches, with inter- and transgranular cracking, Figure 13c. These crack branches are likely to occur at slip planes.



(a) SEM observation along the crack path, red rectangles correspond to EBSD analysis



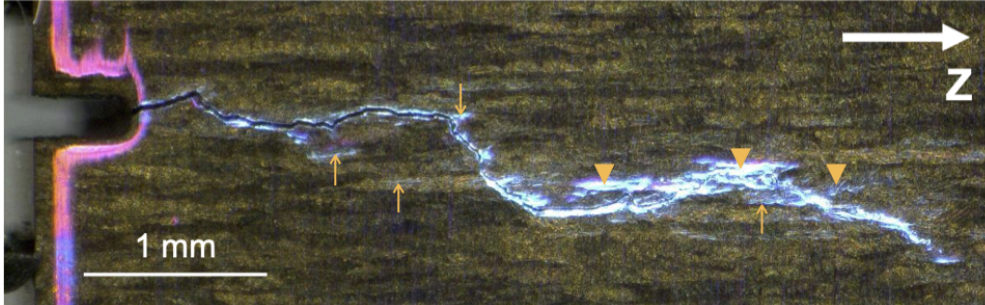
(b) IPF-Z close to the notch, corresponding to label ① in (a)



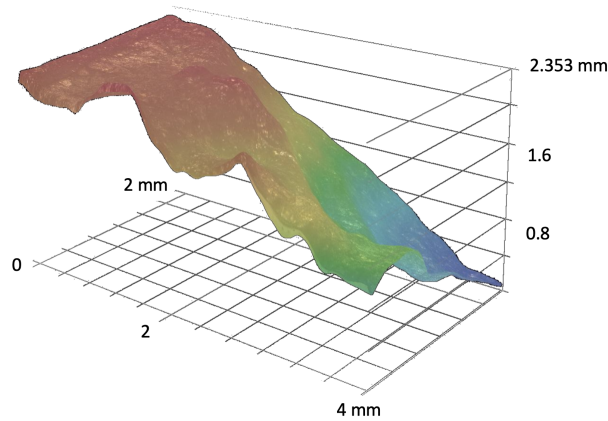
(c) IPF-Z at 2.6 mm from the notch, corresponding to label ② in (a)

Figure 13: Crack path of FH-A specimen (a) SEM (secondary electrons) after slight polishing of the surface; (b) and (c) IPF-Z associated to labels in (a)

In addition to these observations, another FH-A specimen was used to obtain in-situ optical images, used in the sequel for numerical analysis. Several micro-cracks were found in the vicinity of the main crack, together with strain localizations patterns which size were consistent with the grain size, Figure 14a. Optical profilometer measurements of the fracture surface shows that these crack oscillations are limited to approximately one third of the specimen thickness, Figure 14b.



(a) In situ optical observation of FH-A specimen



(b) Fractography of FH-A specimen (notch is at abscissa zero)

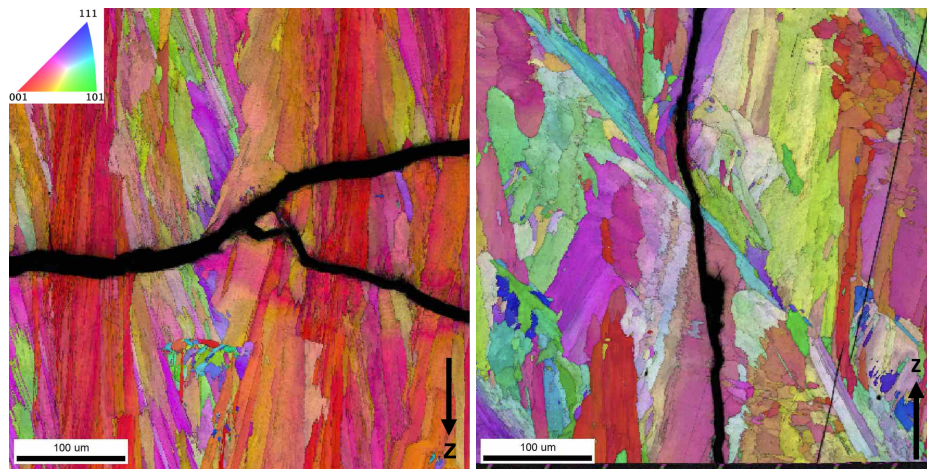
Figure 14: Global fatigue crack path for FH-A sample (a) in situ side view (arrows correspond to some strain localization at grain boundaries and triangles correspond to some strain localization within grains), (b) 3D measurement of crack surface

The crack twisting is clearly more pronounced for FH-A specimen compared to the FV-A specimen (55° and 10° respectively, see Table 6). The amplitude of twisting is also evidenced from side to side in Figures 14b and 10d: the final differences in height being of about 2.3 mm and 1 mm respectively for FH-A and FV-A specimens. The increase in crack twisting with the crack length for the FH-A specimen, associated to its rotation around its main direction of propagation, confirms that the first stage of crack growth is mainly intergranular while it is a mix between inter- and transgranular mechanisms when the crack becomes longer. Conversely the crack for FV-A specimen can be assumed to be mostly driven by transgranular mechanism.

As a conclusion, the crack path is a function of the orientation of loading with respect to the building direction. With the exception of the FV-A case, where cracking is transgranular, the crack growth mechanism appears to be mostly intergranular with crack branches that could be associated to strain localization within grains, and mixing inter- and transgranular cracking mechanisms. These branches did not drive the whole crack path, even though they could yield significant crack oscillations.

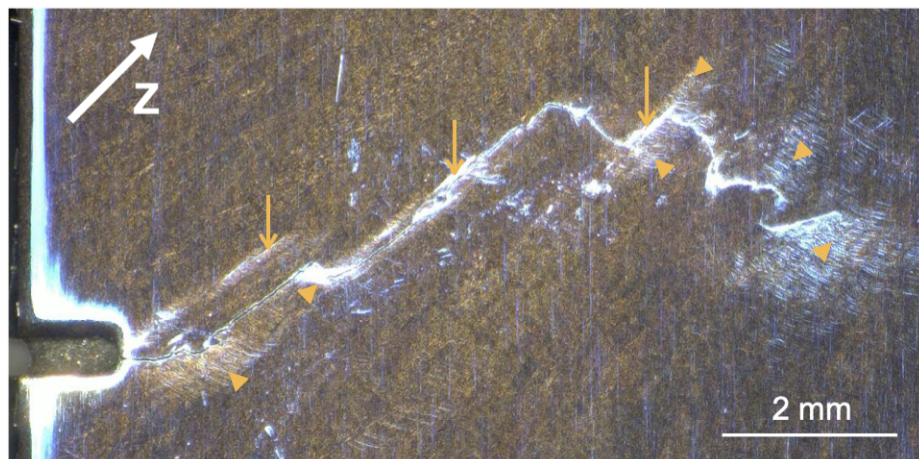
5.2. The "more isotropic" material - set of parameters B

For the set of parameters B, the crack path and crack growth mechanisms are similar to the observations made for the set of parameters A, Figure 15.

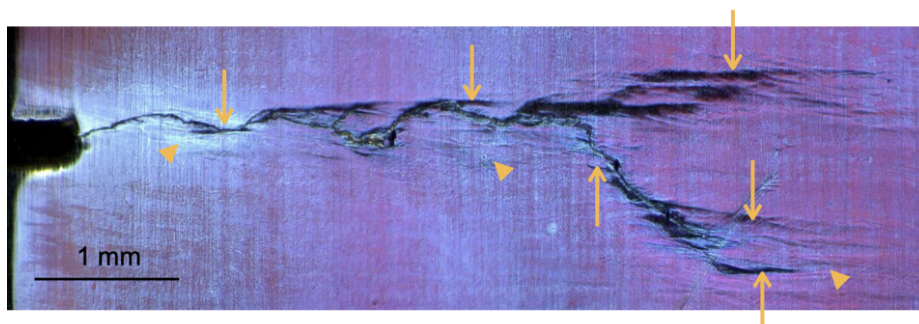


(a) IPF-Z for FV-B

(b) IPF-Z for F45-B



(c) Optical observation for F45-B



(d) Optical observation for FH-B

Figure 15: Crack paths for set of parameters B (orange arrows correspond to some grain boundaries where strain localization and/or cracking occur, and orange triangles correspond to slip lines within grains in (c) and (d))

The FV-B sample yields to a crack orthogonal to the loading direction, exhibiting a transgranular mechanism, Figure 15a. Despite some local crack branches, with slight contribution of intergranular mechanisms, secondary cracks are arrested. For the F45-B sample, the crack path evolves towards 45° angle with respect to the loading direction,

Figure 15c. However, the number of crack deviation and the level of plastic activity are higher compared to F45-A, see Figures 15c and 12. As already observed for F45-A, the crack is close to grain boundaries, irrespective of the crossing of small grains, Figure 15b.

For FH-B specimen, crack is mostly orthogonal to the loading direction, Figure 15d. However, the FH-B specimen exhibit larger tilt and twist angles compared to FH-A (see the lower crack branch in Figure 15d). The cracking mechanisms is again clearly mostly intergranular.

6. Fatigue crack growth assessed by FEA

Because of the complex 3D-shape of the crack path, the SIF values can no longer be derived from analytical standard formulation of shape function for SENT, see eq. 1. Indeed, as soon as the crack deviates from the plane orthogonal to the loading direction, multiaxial local loading and subsequent modal mixity has to be accounted for [44, 45]. Besides, the evidenced elastic anisotropy of the L-PBF IN718 alloy prescribes the use of contour integral J instead of SIF values [46, 47], avoiding by this way complex analysis of SIF modification due to this anisotropy [48, 49]. Thus we propose to consider a simple but realistic crack morphology, and to use J values derived from $G-\theta$ to describe crack driving forces.

6.1. Crack morphology and growth

To account for the complex morphology of the crack path, a spline interpolation of the measured crack path has been carried out. To consider crack twisting, the spline interpolant is determined on crack paths measured on both lateral sides of the specimen. For sake of simplicity, the 3D surface crack model is obtained by a linear interpolation between both spline curves, the crack front being assumed to be straight. This hypothesis is supported by the optical profilometer measurements shown in Figures 14b and 10d. As a mean of comparison, compare the modeled crack surface shown in figure 16a to the real crack surface shown in 14b.

Using this modeled crack surface, it is possible to account for the modal mixity induced by crack tilting (assessed locally on the external surfaces) and twisting (assessed globally from side to side), impacting to a large extent the driving forces for crack growth [45]. A 3D mesh of the modeled crack, using surface elements, has been inserted in the initial SENT mesh derived from computer-aided design (CAD) using conform remeshing technique [45, 27]. The minimum size of the element h is set to $10\ \mu\text{m}$.

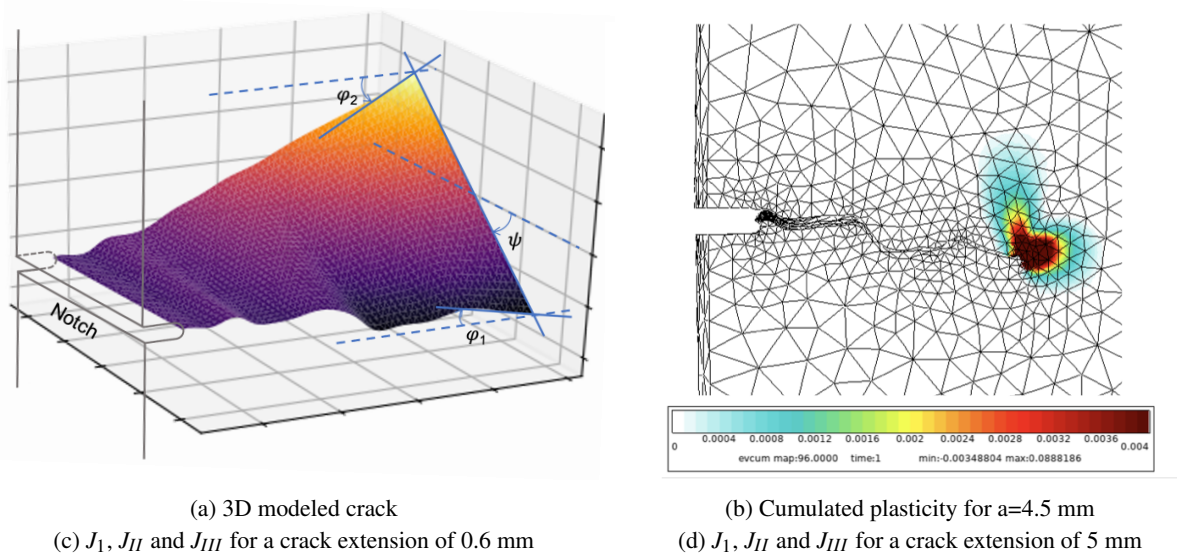


Figure 16: Modelling of FH-A specimen

To analyze the fatigue crack growth in respect to the experimental crack path, front locations have been successively meshed for about ten cracks locations, for crack increments of about 400 μm . The mechanical behavior corresponds to the proposed anisotropic model for elastic and viscoplastic behavior described above. A penalty contact algorithm has been used between crack lips, but friction was neglected. A single cycle has been computed for each crack location in order to limit the computation time. This enables to account for the crack closure effect induced by plasticity, impacting crack closure.

For the FH-A specimen, a clear illustration of the impact of anisotropic behavior and complex 3D crack morphology is given in Figure 16b: the resulting field of cumulated plasticity is fully asymmetric, despite a slight deviation of the crack on the observed side of the specimen. This point is consistent with the loss of symmetry observed in plastic activity in Figure 12.

6.2. Driving forces assessed from $G-\theta$

Using the sample FH-A as an example, J_i values are plot as a function of the location of point from surface to surface described by the abscissa x , where $x=0$ corresponds to the middle of the specimen, see Figures 16c and 16d. These figures correspond respectively to a small crack extension, close to the notch, and a large crack extension, close to the end of the crack growth. For these crack locations, it is obvious that shear mode is at a very high level, the J_{II} value increasing as compared to J_I with crack extension. Besides, edge effects with high local gradient are observed for J_I , J_{II} and J_{III} values, limiting their robustness if assessed in subsurface. This is the reason why we chose to analyze averaged values of J_i along the crack front. The large values of shear modes, and mainly of J_{II} , have also pushed the need to account for modal mixity using a quadratic analysis of J_i described as ΔJ_{eq} considering in fatigue the amplitude of each mode as follows [50]:

$$\Delta J_{eq} = \sqrt{\overline{\Delta J_I^2} + \overline{\Delta J_{II}^2} + \overline{\Delta J_{III}^2}} \quad (4)$$

where $\Delta J_I = J_{I,\max} - \langle J_{I,\min} \rangle$, with $\langle . \rangle$ corresponding to the Macaulay brackets, i.e. $\langle J_{I,\min} \rangle = J_{I,\min}$ if $J_{I,\min} > 0$ and $\langle J_{I,\min} \rangle = 0$ otherwise, the negative values of J_{II} and J_{III} being accounted for, using $\Delta J_{II} = J_{II,\max} - J_{II,\min}$ and $\Delta J_{III} = J_{III,\max} - J_{III,\min}$. Finally, the values $\overline{\Delta J_i}$ (for $i=I, II$ and III) used in ΔJ_{eq} correspond to averaged values along the whole crack front, for each crack length and associated front location. This option should be seen as an efficient way to account for modal mixity induced by crack path, assuming equivalent contribution of each mode in crack growth.

6.3. Fatigue crack growth rate for DS-like material: influence of the orientation

To investigate the role of orientation for high level of anisotropy, firstly the set of Parameters-A material is investigated. The curvilinear crack length a has been experimentally determined from the measured surface crack location as a function of the number of cycles. The potential drop technique is used to obtain continuous measurement of cracked surface. The Fatigue crack growth rate (FCGR) corresponds to the crack increment Δa associated to a given increment of cycles ΔN , and is assumed to be consistent with a Paris' law using ΔJ_{eq} instead of ΔK (similarly to [46]), namely:

$$\frac{da}{dN} \simeq \frac{\Delta a}{\Delta N} = C^* (\Delta J_{eq})^{m^*} \quad (5)$$

Results are shown in Figure 18. The maximum FCGR is reached for the FV-A sample, mostly associated to transgranular cracking. The minimum FCGR is reached for the FH-A and F45-A samples, i.e. for intergranular cracking. Note that similar values are obtained for FH-A and F45-A samples. No short crack behavior is observed for these cases. In addition to these observations, it is interesting to compare this L-PBF IN718 to its wrought counterpart. The FCGR behavior deduced from Paris' law identified for the wrought IN718 at the same temperature was investigated by Clavel et al. [51]. The J values and modified coefficient using a Paris' law formulated in ΔJ , are deduced from ΔK identified in the cited work, see AppendixB. All FCGR data together with crack tilting and twisting angles are detailed in Table 6.

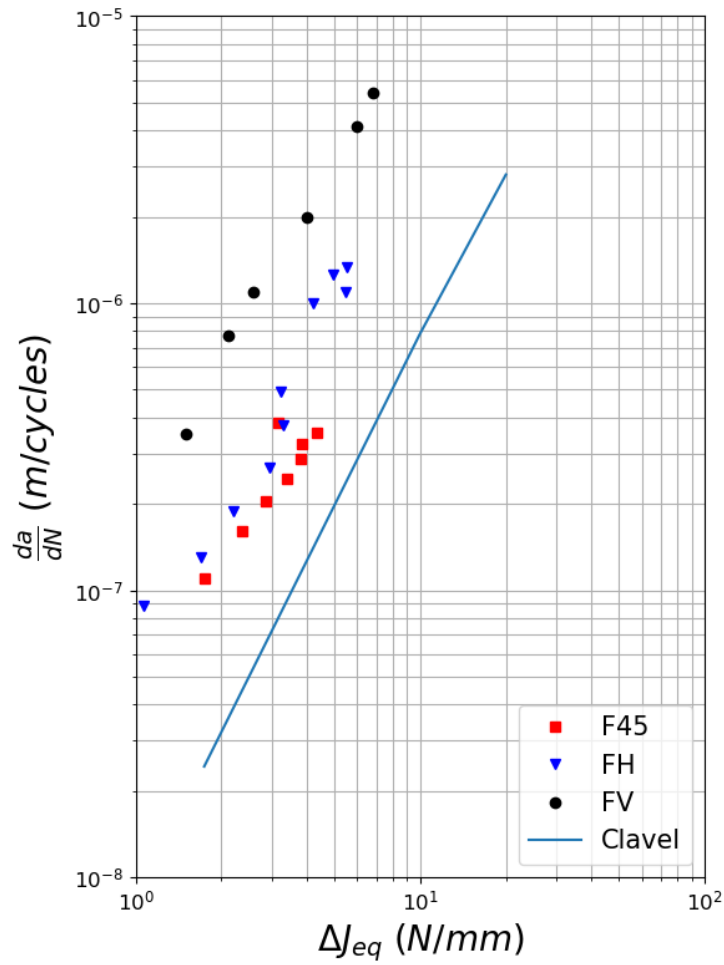


Table 6: SENT samples names and geometry, Paris' law parameters are expressed on the basis of ΔJ_{eq} ; crack tilt and twist angles are measured at the end of the propagation for a crack length of 5 mm. The crack tilt angle corresponds to the angle between crack path observed on both sides (ϕ_1 and ϕ_2) and the direction orthogonal to the loading direction. The crack twist angle (ψ) corresponds to the angle between crack front observed from side to side and the direction orthogonal to the loading direction; see Figure 16(a). (*) *Nota:* for F45-B the values correspond to $J < 4 \text{ Nmm}^{-1}$.

Specimen	Parameters	Paris' law		Tilt angle (°)		Twist angle (°)
		m^*	C^*	ϕ_1	ϕ_2	ψ
FV	A	2	$1.5 \cdot 10^{-7}$	10	0	10
	B	0.65	$8.0 \cdot 10^{-8}$	0	15	15
F45	A	1.48	$7.4 \cdot 10^{-8}$	45	60	15
	B (*)	0.95	$5.0 \cdot 10^{-7}$	30	50	80
FH	A	2	$4.0 \cdot 10^{-8}$	20	35	55
	B			50	25	30
from [51]	Cast	1.9	$9.6 \cdot 10^{-9}$	-	-	-

6.4. The role of AM anisotropic microstructure on fatigue crack growth rate

The FV-B specimen, characterized by transgranular cracking, leads to a drastic lowering of FCGR compared to FV-A, Figure 18a.

On the other hand, the observed FCGR for FH specimens, associated to intergranular cracking, are similar regardless of the processing parameters, see Figures 18c and 14, despite clear differences in both texture and grains morphology, Figures 5. The observed FCGR for FH specimens yields to a Paris regime, although clearly higher than the wrought IN718. The FCGR has been identified for this intergranular mechanism, and yields $m^* = 2$ and $C^* = 4 \cdot 10^{-8}$. The FCGR for the F45-A specimen is very similar to this identification, see Figure 18b where the dashed black curve corresponds to the identification made for FH specimens. Thus, an intrinsic FCGR for intergranular mechanisms seems being reached. However, this does not hold true for the F45-B specimen despite its intergranular crack growth. Indeed, its FCGR is much lower than the trend observed for FH-A, FH-B and F45-A. This can be explained by the higher number of crack deviations in F45-B, yielding to a more tortuous crack path for this specimen as compared to F45-A. Besides, the large number of strain localization areas could also impede the crack growth, Figure 15(c).

The major differences between both set of parameters are associated to the grain morphology and the crystallographic orientations of the apparent microstructures in the plane orthogonal to the Z-direction. In a nutshell, Parameters-A is very similar to a directionally solidified alloy for which $\langle 001 \rangle$ orientation is dominant in the building direction, which is known to be very sensitive in FCGR to the specimen orientation, see for instance for Ni base DS superalloy the case of MARM200 [52]. However, in this case authors stressed out that the higher the elastic modulus, the higher the FCGR was observed, which is clearly not the case in our study, see Figure 18: the highest elastic modulus being associated to F45 specimens.

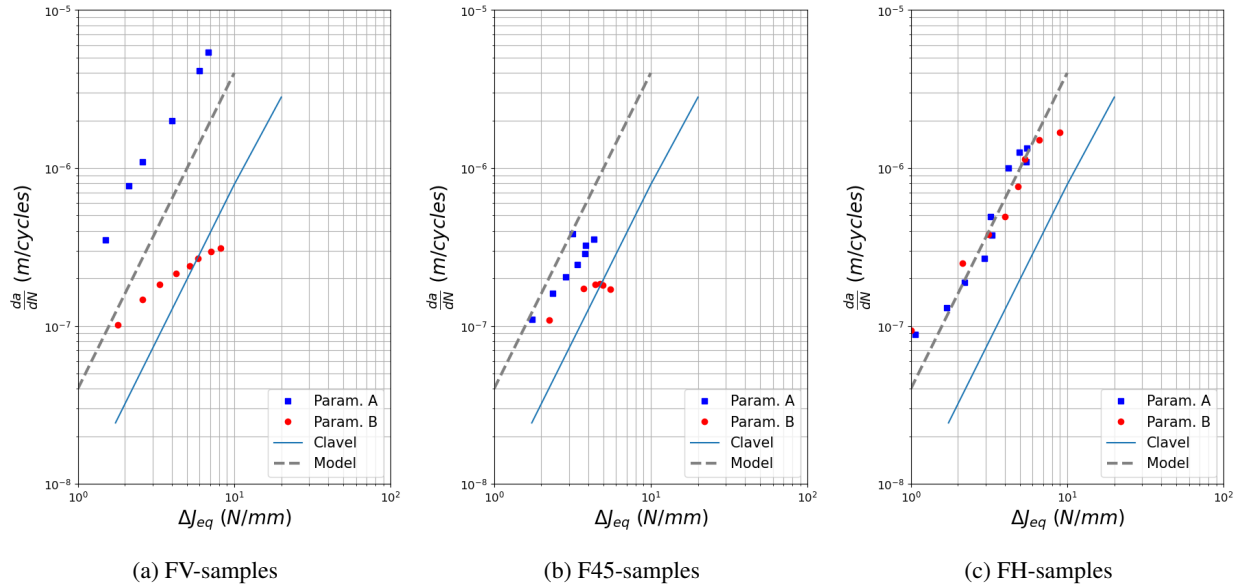


Figure 18: FCGR as a function of ΔJ_{eq} for set of parameters A and B for different samples orientations (Clavel corresponds to wrought IN718 [51] and model corresponds to Paris law identified for FH specimens in this study)

Thus, these results strongly suggests that there is an intrinsic FCGR related to the intergranular crack growth mechanism. On the other hand, the FCGR for the transgranular crack growth mechanism appears to be strongly dependent on the microstructure. If proven true, this could have important implications for the design of parts, from the choice of processing conditions to the orientations of the part with respect of the building direction.

There are, however, a possibility that the modeling strategy used in this study oversimplifies the crack to microstructure interaction in different aspects: i) no friction between crack lips is described, which could impact the obtained ΔJ values especially for shear modes, ii) the linear interpolation between each crack paths on surfaces ignores the potential impact of local roughness within the specimen, and iii) the homogeneous assumption used for mechanical behavior ignores local plasticity within each grain, a crystal plasticity model being a possibility to describe this effect [43]. These methods are however costly and beyond the scope of this study. It is also worth noting that neither the real crack morphology nor the crack front have been accounted for, whereas it has been evidenced that this could impact local FCGR especially for local high curvature of the crack front [53, 45]. More experimental investigations, probing the effect of other microstructures obtained by additive manufacturing, are thus necessary to confirm the observed trends.

7. Conclusion

In this study, two microstructures exhibiting different grain morphologies and crystallographic textures, but low porosity, were build using L-PBF. One microstructure was found to exhibit a degree of anisotropy close to a directionally solidified alloy, while the other was more isotropic. The mechanical behavior of these materials was successfully modeled by homogeneous orthotropic elasticity, Hill's criterion and combination of kinematic hardenings.

No evidence of crack to pores interaction has been observed during fatigue tests. Both crack path and fatigue crack growth rate are sensitive to the chosen orientation of specimen and notch according to the processing direction. Fatigue crack growth is intergranular in nature regardless of the loading direction, with the exception of the case where the loading direction and the building direction are aligned. In this last case, transgranular cracking was dominant.

As a major result, it has been evidenced no or limited effect of processing parameters when the crack growth is intergranular. Indeed, the FCGR in this case is only weakly dependent on the microstructure. On the other hand, the FCGR is driven by the microstructure when the crack growth is transgranular. As such, the highest FCGR for one set of parameters corresponds to the transgranular case, while it is the intergranular case for the other set of parameters.

This has serious implication for the printing strategy of parts, since it shows that FCGR are directly related to the orientation of the notch (similarly to crack initiation site) with respect to the building orientation. There is thus a crucial need for tolerance damage analysis to account for the processed microstructure in intermediate orientations.

Finally, these findings highlight that the combination of fatigue crack growth testing with 3D FEA with explicit model of crack morphology, is a powerful tool to clarify damage mechanisms in complex materials. A G- θ analysis was here justified by the strong mechanical anisotropy, often ignored in literature dealing with fatigue crack growth analysis for AM alloys. In addition to these aspects, even though large grains compared to crack size questions the use of homogeneous behavior model, the chosen anisotropic criteria gives access to sounded analysis of this anisotropy in presence of a crack accounting for complex crack closure effect in 3D. This allows the identification of an intrinsic FCGR associated to either trans- or intergranular dominant mechanism in fatigue crack growth.

AppendixA. Shear mode from G- θ

Using J-integral, the complete analysis of crack for any mode is related to the following equation considering homogeneous material [31]:

$$J_k = \int_{\Gamma_N} \left(\frac{1}{2} \sigma_{mn} u_{m,n} n_k - \sigma_{ij} n_j u_{i,k} \right) d\Gamma - \int_{\bar{\Gamma}_N} [[W]]^+ n_k d\Gamma \quad (\text{A.1})$$

in which the term $\int_{\bar{\Gamma}_N} [[W]]^+ n_k d\Gamma$ corresponds to the extra contribution of crack lips, described by surface $\bar{\Gamma}_N$, needed to insure path independence for shear modes along any contour Γ .

In the proposed simplified analysis by G- θ , this contribution has been voluntarily omitted for sake of complex implementation of this term. This induces the loss of the invariance of G_{II} and G_{III} terms as a function of the chosen domain for integration as developed in equation 2. To assess the evolution of G_{II} and G_{III} terms as a function of the chosen domain, the case Parameters -A FH detailed above is used for a single crack front location, Figure A.19.

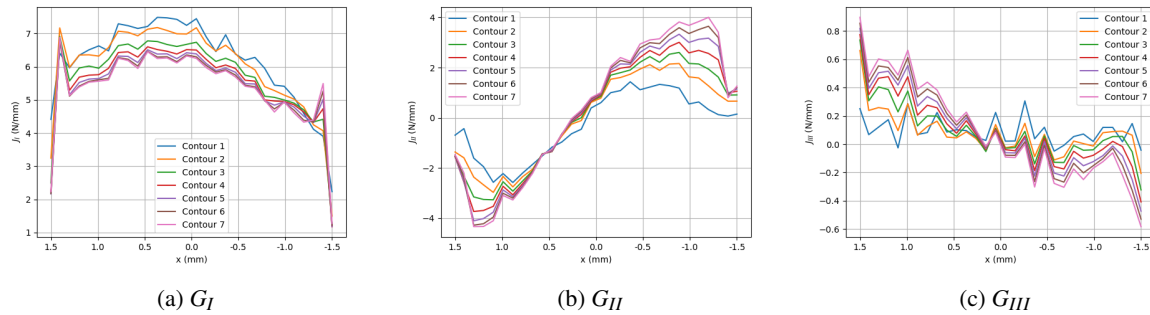


Figure A.19: Evolutions of G_I , G_{II} and G_{III} along the crack front and function of the chosen domain for volume integral obtained by G- θ ; the higher the number, the higher the distance to the crack tip. Plots correspond to the maximum applied stress.

If one considers only 4 layers of elements (contour 4) for domain integration, the associated values of G_{II} and G_{III} terms along the crack front is shown to evolve with the chosen domain. Values reached for 7 contours still evolve for shear modes, but seem to be correlated to a slighter evolution. Whereas for mode I, the convergence is reached after 4 to 5 contours. The contour 5 is kept in this study, corresponding to a distance to the crack tip higher than 250 μm .

AppendixB. Analysis of Paris' law from data formulated in ΔK to ΔJ

For comparison purpose, we need to derive Paris' law formulated in ΔK in [51] to ΔJ consistently with the numerical scheme developed above. The J values have been evaluated through Irwin's formula:

$$G = \frac{K^2}{E/(1-\nu^2)} \quad (\text{B.1})$$

where $E=180$ GPa and $\nu=0.3$ corresponding respectively to the Young's modulus and the Poisson's coefficient of wrought IN718 at the considered temperature of 550 °C. This formula corresponds to plane strain condition. The equivalence in terms of Paris's law being:

$$\frac{da}{dN} = C(\Delta K)^m = C^*(\Delta J)^{m^*} \quad (\text{B.2})$$

with $m^* = m/2$ for sake of consistency with equation B.1.

Acknowledgements

This work is dedicated to the memory of our lost friend Alain Koster (1964-2021). The authors warmly acknowledge Jean-Dominique Bartout and Christophe Colin for helping and advising in L-PBF processing and Vincent Chiaruttini (ONERA) for helping in G- θ analysis. Yazid Madi and Kais Ammar are acknowledged for their kind helps for anisotropy plot.

- [1] C. Rans, J. Michielssen, M. Walker, W. Wang, et al., Beyond the orthogonal: On the influence of build orientation on fatigue crack growth in slm ti-6al-4v, *International Journal of Fatigue* 116 (2018) 344–354.
- [2] M. Zavala-Arredondo, T. London, M. Allen, T. Maccio, S. Ward, D. Griffiths, A. Allison, P. Goodwin, C. Hauser, Use of power factor and specific point energy as design parameters in laser powder-bed-fusion (l-pbf) of alsil0mg alloy, *Materials & Design* 182 (2019) 108018.
- [3] M. Ni, C. Chen, X. Wang, P. Wang, R. Li, X. Zhang, K. Zhou, Anisotropic tensile behavior of in situ precipitation strengthened inconel 718 fabricated by additive manufacturing, *Materials Science and Engineering: A* 701 (2017) 344–351.
- [4] K. Moussaoui, W. Rubio, M. Mousseigne, T. Sultan, F. Rezai, Effects of selective laser melting additive manufacturing parameters of inconel 718 on porosity, microstructure and mechanical properties, *Materials Science and Engineering: A* 735 (2018) 182–190.
- [5] L. Lacoste, A. Sakly, S. Dépinoy, S. Lebel, B. Vayre, C. Colin, Microstructure control of additively manufactured in718 by l-pbf process, *Powder Metallurgy* (2022) 1–8.
- [6] D. T. Ardi, L. Guowei, N. Maharjan, B. Mutiargo, S. H. Leng, R. Srinivasan, Effects of post-processing route on fatigue performance of laser powder bed fusion inconel 718, *Additive Manufacturing* 36 (2020) 101442.
- [7] C. Körner, M. Ramsperger, C. Meid, D. Bürger, P. Wollgramm, M. Bartsch, G. Eggeler, Microstructure and mechanical properties of cmsx-4 single crystals prepared by additive manufacturing, *Metallurgical and Materials Transactions A* 49 (9) (2018) 3781–3792.
- [8] L. M. B. Ormastroni, I. Lopez-Galilea, J. Pistor, B. Ruttert, C. Körner, W. Theisen, P. Villechaise, F. Pedraza, J. Cormier, Very high cycle fatigue durability of an additively manufactured single-crystal ni-based superalloy, *Additive Manufacturing* (2022) 102759.
- [9] V. P. Sabelkin, G. R. Cobb, T. E. Shelton, M. N. Hartsfield, D. J. Newell, R. P. O'Hara, R. A. Kemnitz, Mitigation of anisotropic fatigue in nickel alloy 718 manufactured via selective laser melting, *Materials Design* 182 (2019) 108095. doi:<https://doi.org/10.1016/j.matdes.2019.108095>.
URL <https://www.sciencedirect.com/science/article/pii/S0264127519305337>
- [10] K. Gruber, P. Szymczyk-Ziółkowska, S. Dziuba, S. Duda, P. Zielonka, S. Seitl, G. Lesiuk, Fatigue crack growth characterization of inconel 718 after additive manufacturing by laser powder bed fusion and heat treatment, *International Journal of Fatigue* (2022) 107287.
- [11] X. Ma, H. Zhai, L. Zuo, W. Zhang, S. Rui, Q. Han, J. Jiang, C. Li, G. Chen, G. Qian, et al., Fatigue short crack propagation behavior of selective laser melted inconel 718 alloy by in-situ sem study: Influence of orientation and temperature, *International Journal of Fatigue* 139 (2020) 105739.
- [12] S. Lynch, T. Radtke, B. Wicks, R. Byrnes, Fatigue crack growth in nickel-based superalloys at 500-700° c. ii: Direct-aged alloy 718, *Fatigue & Fracture of Engineering Materials & Structures* 17 (3) (1994) 313–325.
- [13] J. Pedron, A. Pineau, The effect of microstructure and environment on the crack growth behaviour of inconel 718 alloy at 650 c under fatigue, creep and combined loading, *Materials science and engineering* 56 (2) (1982) 143–156.
- [14] F. Alexandre, S. Deyber, A. Pineau, Modelling the optimum grain size on the low cycle fatigue life of a ni based superalloy in the presence of two possible crack initiation sites, *Scripta Materialia* 50 (1) (2004) 25–30.
- [15] A. Nicolay, J.-M. Franchet, N. Bozzolo, J. Cormier, Metallurgical analysis of direct aging effect on tensile and creep properties in inconel 718 forgings, in: *Superalloys 2020*, Springer, 2020, pp. 559–569.
- [16] M. Abikchi, T. Billot, J. Crépin, A. Longuet, C. Mary, T. F. Morgeneyer, A. Pineau, Fatigue life and initiation mechanisms in wrought inconel 718 da for different microstructures, in: *13th international conference on fracture*, 2013, pp. 11–p.
- [17] L. Doremus, J. Cormier, P. Villechaise, G. Hénaff, Y. Nadot, S. Pierret, Influence of residual stresses on the fatigue crack growth from surface anomalies in a nickel-based superalloy, *Materials Science and Engineering: A* 644 (2015) 234–246.
- [18] N. Kouraytem, J. Varga, B. Amin-Ahmadi, H. Mirmohammad, R. A. Chanut, A. D. Spear, O. T. Kingstedt, A recrystallization heat-treatment to reduce deformation anisotropy of additively manufactured inconel 718, *Materials & Design* 198 (2021) 109228.
- [19] A. Koster, E. Fleury, E. Vasseur, L. Remy, Thermal-mechanical fatigue testing. in: *Automation in fatigue and fracture: Testing and analysis* (edited by c. amzallag), ASTM STP 1231 (1994) 563–580.
- [20] F. Szymtka, L. Remy, H. Maitournam, A. Koster, M. Bourgeois, New flow rules in elasto-viscoplastic constitutive models for spheroidal graphite cast-iron, *International Journal of Plasticity* 26 (6) (2010) 905 – 924. doi:10.1016/j.ijplas.2009.11.007.
URL <http://www.sciencedirect.com/science/article/pii/S0749641909001612>
- [21] S. Dezecot, M. Rambaudon, A. Koster, F. Szymtka, V. Maurel, J.-Y. Buffiere, Fatigue crack growth under large scale yielding condition in a cast automotive aluminum alloy, *Materials Science and Engineering: A* 743 (2019) 87–97.
- [22] ASTM E647-15 Standard Test Method for Measurement of Fatigue Crack Growth Rates, ASTM International, 2015.

- [23] F. Soniak, Fissuration en fatigue d'un superalliage de la métallurgie des poudres, l'astroloy: influence de la longueur de fissure et de la température, Ph.D. thesis, Ecole Nationale Supérieure des Mines de Paris (1989).
- [24] G. Shen, J. A. Gianetto, W. R. Tyson, Measurement of jr curves using single-specimen technique on clamped se (t) specimens, in: The nineteenth international offshore and polar engineering conference, OnePetro, 2009.
- [25] C. Bassindale, X. Wang, W. Tyson, S. Xu, Numerical verification of stress intensity factor solution for clamped single edge notched tension (sent) specimens, *Fatigue & Fracture of Engineering Materials & Structures* 41 (2) (2018) 494–499.
- [26] V. Maurel, A. Koster, L. Remy, M. Rambaoudon, D. Missoum-Benziane, V. Fontanet, F. Salgado-Goncalves, A. Heudt, H. Wang, M. Trabelsi, Fatigue crack growth under large scale yielding condition: the need of a characteristic length scale, *International Journal of Fatigue* 102 (2017) 184–201. doi:10.1016/j.ijfatigue.2017.03.021.
- [27] Zset software, non-linear material & structure analysis suite, <http://www.zset-software.com>.
- [28] P. Destuynder, M. Djaoua, S. Lescure, Quelques remarques sur la mécanique de la rupture élastique, *Journal de Mécanique Théorique et Appliquée* 2 (1) 113–135.
- [29] O. Kolednik, R. Schöngundner, F. Fischer, A new view on j-integrals in elastic-plastic materials, *International Journal of Fracture* 187 (1) (2014) 77–107.
- [30] V. Maurel, V. Chiaruttini, A. Koster, D. Missoum-Benziane, Fatigue crack growth under large scale yielding condition: a tool based on explicit crack growth, *Journal of Theoretical, Computational and Applied Mechanics*.
- [31] A. Vattré, Kinked and forked crack arrays in anisotropic elastic bimetals, *Journal of the Mechanics and Physics of Solids* 160 (2022) 104744.
- [32] O. Andreau, I. Koutiri, P. Peyre, J.-D. Penot, N. Saintier, E. Pessard, T. De Terris, C. Dupuy, T. Baudin, Texture control of 316l parts by modulation of the melt pool morphology in selective laser melting, *Journal of Materials Processing Technology* 264 (2019) 21–31.
- [33] S. Dépinoy, Influence of solidification conditions on chemical heterogeneities and dislocations patterning in additively manufactured 316l stainless steel, *Materialia* (2022) 101472.
- [34] F. Povo, J. Reggiardo, Stress-relaxation in bending of inconel 718, at 773 and 823 k, *Journal of materials science* 23 (1) (1988) 241–247.
- [35] R. Hill, Constitutive modelling of orthotropic plasticity in sheet metals, *Journal of the Mechanics and Physics of Solids* 38 (3) (1990) 405–417.
- [36] R. Hill, *The mathematical theory of plasticity*, Vol. 11, Oxford university press, 1998.
- [37] R. De Borst, P. H. Feenstra, Studies in anisotropic plasticity with reference to the hill criterion, *International journal for numerical methods in engineering* 29 (2) (1990) 315–336.
- [38] H. Lin, H. Nayeb-Hashemi, R. M. Pelloux, Constitutive relations and fatigue life prediction for anisotropic al-6061-t6 rods under biaxial proportional loadings, *International journal of fatigue* 14 (4) (1992) 249–259.
- [39] J. L. Chaboche, P. M. Lesne, A non-linear continuous fatigue damage model, *Fatigue and Fracture of Engineering Materials and Structures* 11 (1988) 1–17.
- [40] J. Lemaitre, J. L. Chaboche, *Mechanics of Solid Materials*, Cambridge University Press, 1990.
- [41] H. Farooq, G. Cailletaud, S. Forest, D. Ryckelynck, Crystal plasticity modeling of the cyclic behavior of polycrystalline aggregates under non-symmetric uniaxial loading: Global and local analyses, *International Journal of Plasticity* 126 (2020) 102619.
- [42] A. Cruzado, J. LLorca, J. Segurado, Modeling cyclic deformation of inconel 718 superalloy by means of crystal plasticity and computational homogenization, *International Journal of Solids and Structures* 122 (2017) 148–161.
- [43] F. Coudon, G. Cailletaud, J. Cormier, L. Marcin, A multiscale model for nickel-based directionally solidified materials, *International Journal of Plasticity* 115 (2019) 1–17.
- [44] M. Abecassis, A. Köster, V. A. Esin, V. Chiaruttini, V. Maurel, Crack growth behavior in dissimilar welded ti based alloys under biaxial fatigue loading, *International Journal of Fatigue* 118 (2019) 209–224.
- [45] V. Maurel, V. Chiaruttini, M. Abecassis, A. Koster, S. Dezecot, Influence of a 3d realistic crack path in the driving forces for fatigue crack growth under mode i+ ii loading, *Theoretical and Applied Fracture Mechanics* 108 (2020) 102570.
- [46] N. E. Dowling, J. A. Begley, Fatigue crack growth during gross plasticity and the j-integral, *Mechanics of Crack Growth*. ASTM, Philadelphia, Pa. 1976.
- [47] S. Chu, C. S. Hong, Application of the jk integral to mixed mode crack problems for anisotropic composite laminates, *Engineering Fracture Mechanics* 35 (6) (1990) 1093–1103.
- [48] P. Sollero, M. Aliabadi, Fracture mechanics analysis of anisotropic plates by the boundary element method, *International Journal of Fracture* 64 (4) (1993) 269–284.
- [49] T. Ikeda, M. Nagai, K. Yamanaga, N. Miyazaki, Stress intensity factor analyses of interface cracks between dissimilar anisotropic materials using the finite element method, *Engineering Fracture Mechanics* 73 (14) (2006) 2067–2079.
- [50] S. Forth, W. Keat, L. Favrow, Experimental and computational investigation of three-dimensional mixed-mode fatigue, *Fatigue & Fracture of Engineering Materials & Structures* 25 (1) (2002) 3–15.
- [51] M. Clavel, A. Pineau, Fatigue behaviour of two nickel-base alloys i: Experimental results on low cycle fatigue, fatigue crack propagation and substructures, *Materials Science and Engineering* 55 (2) (1982) 157–171.
- [52] G. Leverant, T. Strangman, B. Langer, Parameters controlling the thermal fatigue properties of conventionally-cast and directionally-solidified tubular alloys.
- [53] E. Fessler, E. Andrieu, V. Bonnard, V. Chiaruttini, S. Pierret, Relation between crack growth behaviour and crack front morphology under hold-time conditions in da inconel 718, *International Journal of Fatigue* 96 (2017) 17–27.